Turbulent dissipation along contrasting internal tide paths, off the Amazon shelf from AMAZOMIX

Fabius Kouogang[1,5], Ariane Koch-Larrouy[1], Jorge Magalhaes[2], Alex Costa da Silva[4], Daphne Kerhervé[1], Arnaud Bertrand[5], Evan Cervelli[3], Fernand Assene[4], Jean-François Ternon[6], Pierre Rousselot[7], James Lee[8], Marcelo Rollnic[8], Moacyr Araujo[5]

[1]CECI, Université de Toulouse, CERFACS/CNRS/IRD, Toulouse, France

[2]Department of Geoscience, Environment and Spatial Planning (DGAOT), Faculty of Sciences, University of Porto, Porto, Portugal

[3]Rockland Scientific Inc, Lunenburg, Nova Scotia, Canada

[4]Centro Euro-Mediterraneo sui Cambiamenti Climatici, Bologna, Italy

[5]Departamento de Oceanografia, Universidade Federal de Pernambuco, DOCEAN/UFPE, Recife, Brazil

[6]MARBEC, Université de Montpellier, CNRS, Ifremer, IRD, Sète, France

[7]IMAGO, Université de Bretagne Occidentale, CNRS, Ifremer, IRD, Brest, France

[8]Departamento de Oceanografia, Universidade Federal do Pará, UFPA, Belém, Brazil

Correspondence to: Fabius Kouogang (fabius.cedric@yahoo.fr)

Abstract

The Amazon shelf break is a key oceanic region where strong internal tides (ITs) are generated, playing a substantial role in climate processes and ecosystems through vertical dissipation and mixing. During the AMAZOMIX survey (2021), currents, hydrography, and turbulence were measured over the M_2 tidal period (12.42 hrs) at multiple stations along both high (HTE) and low (LTE) tidal energy paths, covering IT generation and propagation regions off the Amazon shelf. This dataset provides a unique opportunity to assess IT-driven vertical dissipation~~mixing~~ and quantify its spatial extent and influence in the region. Microstructure analyses, integrated with hydrographic data, highlighted contrasting dissipation rates. The highest rates occurred at IT generation sites along the HTE paths, while the lowest rates were observed on the slope along the LTE path. Near generation sites, dissipation~~mixing~~ rates were elevated, [10^{-6}] W kg^{-1}, with IT shear contributing ~60%, compared to the mean baroclinic current (MBC) shear. Along IT paths, rates~~mixing~~ decreased to [10^{-8}] W kg^{-1} but remained substantial, driven by nearly equal contributions from IT and MBC shear.

A key finding was the relative increase in turbulent dissipation~~mixing~~ ([10^{-7}] W kg^{-1}) ~ 230 km from two distinct IT generation sites at the shelf break. This zone of high dissipation~~mixing~~ was located in an area where the general circulation vanished, coinciding with a region of potential constructive interference of IT rays originating from different generation sites. It also

aligned with the occurrence of large-amplitude internal solitary waves (ISWs), suggesting that constructive IT ray interference may generate nonlinear ISWs that leadISWs lead to enhanced dissipationmixing.

1 Introduction

Turbulent mixing in the ocean is essential for sustaining thermohaline and meridional overturning circulation and for maintaining the global ocean energy budget (Koch-Larrouy et al., 2010; Kunze, 2017). It regulates climate by controlling heat and carbon transport and providing nutrients for photosynthesis (Huthnance, 1995; Munk & Wunsch, 1998). Mixing effects are often reflected in step-like density features, indicating homogeneous regions (Koch-Larrouy et al., 2015; Bouruet-Aubertot et al., 2018). Ocean mixing can be driven by processes like current shear (Miles, 1961; Rainville and Pinkel, 2006; Whalen et al., 2012), river plumes (Ruault et al., 2020), fronts (Geyer, 1995), overturns (Munk and Wunsch, 1998; Thorpe, 2018), and tides (Zhao et al., 2012).

Barotropic tides interacting with sharp topography generate internal tides (ITs), strong internal waves at tidal frequencies and harmonics (Zhao et al., 2016). ITs can create strong vertical displacements of up to tens of meters (Garrett and Kunze, 2007) and may propagate offshore. As they propagate, ITs can interact with topography, stratification, waves, currents, and eddies (Whalen et al., 2012; Bordois, 2015; Ivey et al., 2020; Inall et al., 2021), leading to complex offshore mixing (Gill, 1982). ITs can also destabilize, break, and dissipate locally (Zhao et al., 2016), and their intensity and path can change due to environmental factors, potentially generating nonlinear Internal Solitary Waves (ISWs; Jackson et al., 2012).

These processes are prominent in the Amazon River-Ocean Continuum (AROC) in the western tropical Atlantic. This dynamic region, shaped by interactions between currents, eddies, the Amazon River plume, and internal waves, drives complex circulation and vertical mixing. The North Brazil Current (NBC), the region's dominant western boundary current, flows northwest along the coast (Fig. 1), with velocities of ~1.2 m s^{-1} and a vertical extent of up to 100 m, transporting warm, saline waters from the South Atlantic (Barnier et al., 2001). The NBC influences the Amazon plume's dispersal and contributes to mesoscale eddy formation (Johns et al., 1998; Bourlès et al., 1999; Neto & Silva, 2014). The Amazon plume shows strong seasonal variability, extending up to 1500 km offshore during the rainy season (May–July) and retreating to under 500 km during the dry season (September–November; Coles et al., 2013).

At the Amazon shelf break, internal waves, such as ITs and ISWs, are generated, propagate, and dissipate. These waves have been observed through in situ measurements (Brandt et al., 2002) and SAR satellite imagery (Magalhães et al., 2016). Recently, de Macedo et al. (2023) used MODIS images to identify frequent mode-1 ISWs originating from two IT generation sites (A^a and A^b; Figs. 1, 2a, and 2b), with wavelengths ranging from 72 to 128 km. These ISWs appeared where Tchilibou et al. (2022) predicted IT energy dissipation using numerical modeling. Their findings suggest that ~30% of M_2 IT energy dissipates near the generation sites on the slope (A^a, A^b, and E; Fig. 1), corresponding to higher-mode ITs, while lower-mode ITs propagate offshore, where they dissipate and enhance mixing. Offshore mixing may result from shear instabilities driven by interactions

between currents, eddies, the Amazon plume, ITs, and coupled processes (e.g., wave-wave, wave-current, or plume-wave interactions). However, no direct dissipation measurements have been made in this region to quantify IT-driven mixing.

To address this, the AMAZOMIX cruise (Bertrand et al., 2021) was conducted to investigate IT-driven mixing off the Amazon shelf. Microstructure and hydrographic measurements were collected at repeated stations over an M_2 tidal cycle (~12.42 hrs), providing dissipation estimates and insights into associated processes. Stations were positioned along contrasting IT paths, such as high tidal energy (HTE) paths (sites A^a and A^b; Fig. 1) and low tidal energy (LTE) path (site E; Fig. 1), enabling dissipation quantification in varying tidal regimes. The AMAZOMIX dataset provides a unique opportunity to assess the role of ITs in mixing within the AROC region.

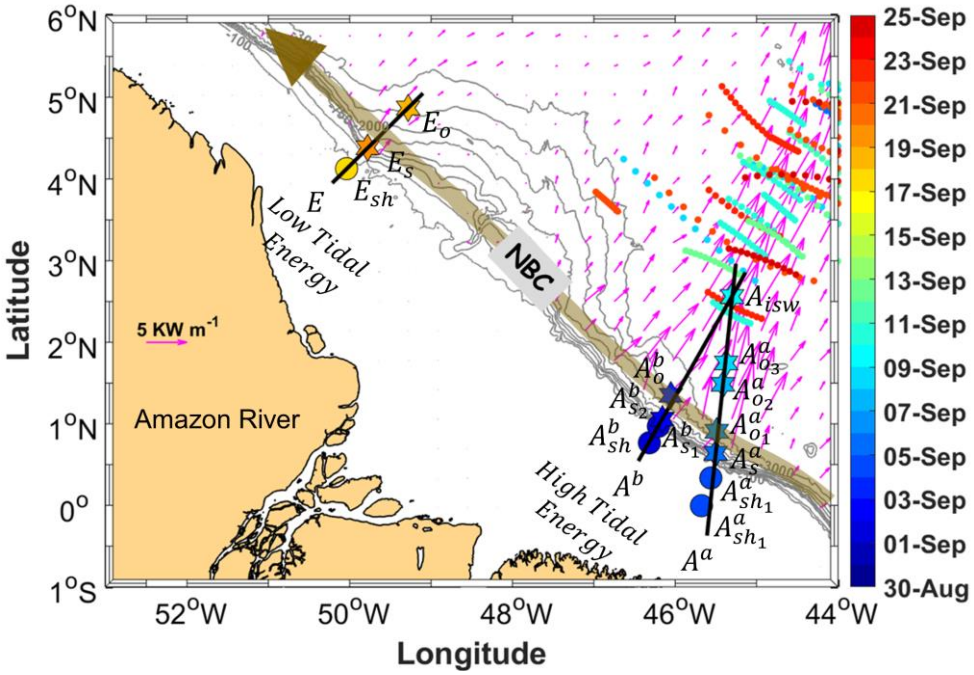

Figure 1: Map of a part of the AMAZOMIX 2021 cruise off the Amazon shelf, showing bathymetric contours (100 m, 750 m, 2000 m, and 3000 m isobaths) in gray. Magenta arrows show the 25-hour mean depth-integrated baroclinic IT energy flux (September 2015, from the NEMO model) originating from IT generation sites (A^a, A^b, and E) along the shelf break. Solid black lines depict transects (A^a, A^b, and E) defined on the high tidal energy (HTE) and low tidal energy (LTE) paths. The solid brown line represents the NBC pathways, illustrating background circulation. Shattered colored lines highlight ISW signatures. Colored circles and stars indicate short and long CTD-O2/L-S-ADCP stations, respectively, with the corresponding sampling dates represented by the color bar. The superscripts "a" and "b" on station names correspond to sites A^a and A^b, respectively. The subscripts "sh", "s", "o", and "isw" indicate station locations: shelf ($A^a_{sh_1}$, $A^a_{sh_2}$, A^b_{sh}, and E_{sh}), slope (A^a_s, $A^b_{s_1}$, $A^b_{s_2}$, and E_s), open ocean ($A^a_{o_1}$, $A^a_{o_2}$, $A^a_{o_3}$, A^b_o, and E_o), and ISW regions (A_{isw}) for sites A^a, A^b and E, respectively.

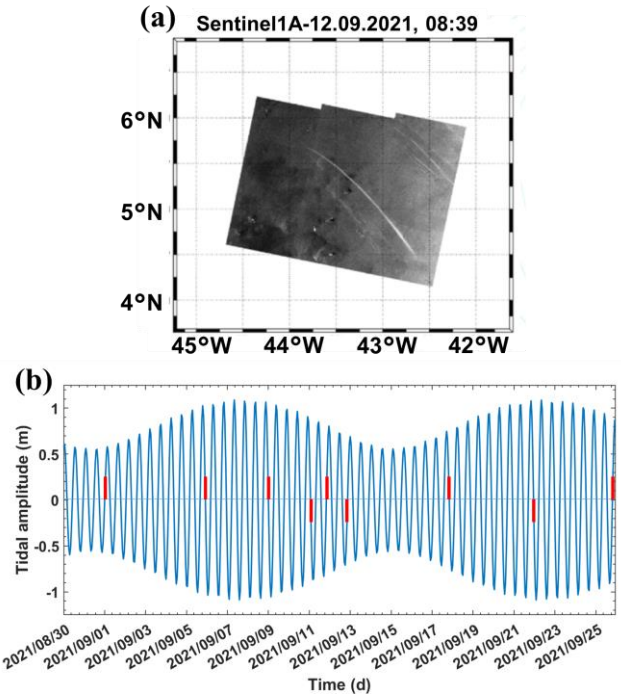

Figure 2: a) 1A Sentinel image acquired on 12th September 2021, showing ISW signatures. b) Tidal (M_2 and S_2) amplitude of the currents (at -45.5°W, 1°N) derived from the FES2014 model (Lyard et al., 2014). ISW signature dates are marked by red bars.

2 Data and Methods

2.1 Data collection

The AMAZOMIX cruise (Bertrand et al., 2021) was performed over the shelf/slope areas off the AROC during August-October 2021 aboard the IRD vessel RV *ANTEA*. At each designated site, 12-hour stations were set up, with repeated casts (4-5 casts per site) of Conductivity-Temperature-Depth-Oxygen (CTD-O_2)/Lowered Acoustic Doppler Current Profiler (LADCP) and Velocity Microstructure Profiler (VMP) to measure the Turbulent Kinetic Energy (TKE) dissipation rates over a complete tidal (M_2) cycle, allowing the separation of the tidal component from the total current. A high-resolution (1/36°) NEMO (Nucleus for European Modeling of the Ocean) model (Madec et al., 2019) was used to determine station locations based on realistic IT

generation and propagation maps (Tchilibou et al., 2022; Assene et al., 2024) and to estimate the mean background stratification. Measurement stations for short- and long-duration (~12 hrs) deployments were systematically named and organized by location along the HTE and LTE paths. Stations at sites A^a and A^b were marked with superscripts "a" and "b", respectively. Subscripts denoted specific regions: "sh" for shelf ($A^a_{sh_1}$, $A^a_{sh_2}$, A^b_{sh}, and E_{sh}), "s" for slope (A^a_s, $A^b_{s_1}$, $A^b_{s_2}$, and E_s), "o" for offshore/open ocean ($A^a_{o_1}$, $A^a_{o_2}$, $A^a_{o_3}$, A^b_o, and E_o), and "isw" for ISW regions (A_{isw}) (Fig. 1; Table A1, Appendix A).

CTD-O_2 measurements were obtained using a Seabird 911 Plus with dual sensors mounted in the rosette. The 24 Hz CTD-O_2 sensors were calibrated before and after the cruise to ensure accurate dissolved oxygen measurements throughout the survey. The temperature, salinity, and oxygen standard deviation, between the CTD-O2 sensors and the bottle samples, was 0.003 °C, 0.003 PSU, and 0.05 ml l^{-1}, respectively. CTD-O_2 data were averaged over 1-m bins to filter out spikes and missing points and aligned in time to correct the lag effects.

Two 300 kHz RDI LADCPs were mounted on the rosette to provide vertical current profiles with 8 m resolution, supplemented by 75 kHz shipboard ADCP (SADCP) profiles recorded continuously during the cruise. Vertical resolution of SADCP was adjusted according to bottom depth, e.g., 8 m for depths >150 m (at $A^b_{s_2}$, A^b_o, A^a_s, A_{isw}, E_s and E_o) and 4 m for other depths. Data processing and quality control followed GO-SHIP Repeat Hydrography Manual protocols. In total, 71 CTD-O_2/LADCP profiles were collected during the AMAZOMIX cruise.

To characterize mixing, the TKE microstructure profiles were obtained from high-frequency (~2 mm resolution) measurements of temperature and velocity shear using a VMP-250 profiler (Rockland Scientific International, Inc.) capable of reaching depths up to 1000 m. The VMP-250 features two high-resolution thermistors (FP07) and two high-resolution velocity shear probes (probes 1 and 2; with 5% signal accuracy), with a sampling rate of 1024 Hz. The profiler was deployed and retrieved via an electric winch and rope tether, with alternating deployments between the CTD-O_2/LADCP profiles at 33 stations, yielding a total of 201 profiles. For this study, data from 14 stations comprising SADCP data, 109 VMP profiles, and 54 CTD-O_2/LADCP profiles will be analyzed.

2.2 Methods

2.2.1 TKE dissipation rates

The VMP data are processed using the ODAS Matlab library (developed by Rockland Scientific International, Inc.) to infer the TKE dissipation rate (ε). The processing methods for the VMP data are briefly described here and adhere to the recommendations of ATOMIX (Analyzing ocean Turbulence Observations to quantify MIXing), as reported by Lueck et al. (2024), and have been validated against the benchmark estimates (presented in Fer et al., 2024).

First, the VMP data are converted into physical shear units, and the time series are prepared. Continuous sections of the time series are selected for dissipation estimation. Before spectral estimation, the aberrant shear signals caused by vessel wake contamination are removed. Collisions of the shear probe with plankton and other particles are removed using the de-spiking routine. The records from each section are then high-pass filtered (e.g., at station $A^b_{s_2}$; Fig. 3).

Shear spectra are estimated using record lengths (L) and Fast Fourier Transform segments of 2 s, which are cosine windowed and overlapped by 50% (e.g., at station $A_{s_2}^b$; Fig. 3). Additionally, vibration-coherent noise is removed. Different L and overlap (O) settings were selected and tested based on the environment (e.g., deep vs. shallow water), following Fer et al. (2024). For shallow stations, L (O) was shortened to 5 s (2.5 s), in contrast to the 8 s (4 s) used for deeper stations, due to evidence of overturns observed in AMAZOMIX acoustic measurements at deeper stations (A. Koch-Larrouy, personal communication, September 20, 2024). This adjustment helped to optimize the spatial resolution of dissipation estimates in shallow water stations.

Finally, ε is determined using the spectral integration method and by comparison with the Nasmyth empirical spectrum (Nasmyth, 1970). Quality assurance tests are carried out in accordance with ATOMIX's recommendations (Lueck et al., 2024). A figure of merit < 1.4 is used to exclude bad data (e.g., at station $A_{s_2}^b$; Fig. 3), and the fraction of data affected by de-spiking is < 0.05.

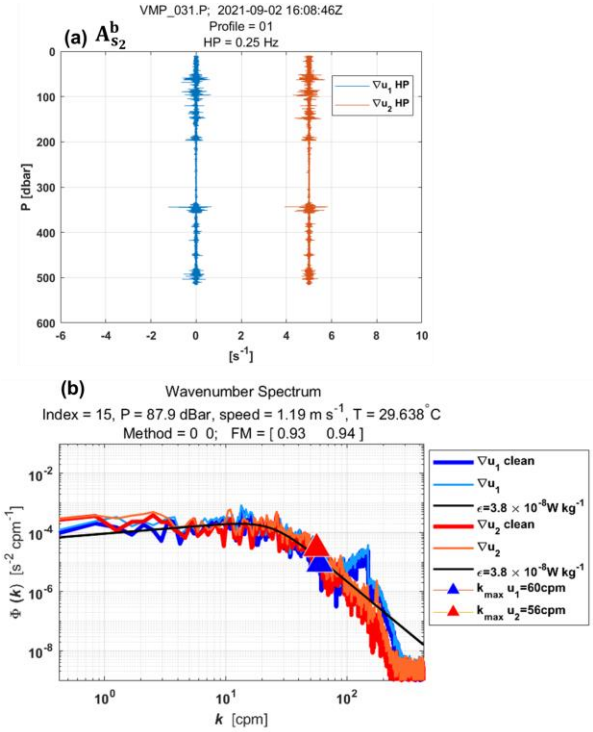

Figure 3: *Example of wavenumber spectra from a dissipation structure segment used to determine the dissipation rate at station $A^b_{s_2}$ at a pressure of 87.9 dBar. (a) Cleaned and high-pass filtered signals from shear probe 1 (blue) and shear probe 2 (red, offset by 5 s^{-1}). (b) Wavenumber spectra for shear probes 1 and 2. Thick lines (blue for probe 1, red for probe 2) show shear spectra with coherent noise correction, while thin lines (sky blue for probe 1, orange for probe 2) show spectra without correction. Triangles mark the maximum wavenumber used for dissipation rate estimation. Black lines represent Nasmyth reference spectra for an estimated dissipation rate of 3.8 x 10^{-8} W kg^{-1} for both shear probes. Dissipation rate estimates for shear probe 1 and shear probe 2 at a pressure of 87.9 dBar yielded a figure of merit of 0.93 and 0.94, respectively*.

Subsurface mixing, driven by IT breaking and shear instabilities, substantially influences the base of the mixed layer, particularly in equatorial waters (Gregg et al., 2003). To analyze midwater dissipation rates (excluding surface and bottom

boundary layers), we define the following depths: Mixed Layer Depth (MLD), miXing Layer Depth (XLD), and Bottom Boundary Layer (BBL) thickness (H_{BBL}).

There are several criteria for defining the MLD. In this study, we use the commonly accepted density threshold criterion of 0.03 kg m^{-3}, as defined by de Boyer Montégut et al. (2004) and Sutherland et al. (2014), to estimate the MLD (Table B1~~A2~~, Appendix B).

The XLD is defined as the depth at which ε decreases to a background level (Sutherland et al., 2014). Previous studies have applied various thresholds for background dissipation levels, such as 10^{-8} and 10^{-9} W kg^{-1} in higher latitudes based on in situ observations (Brainerd and Gregg, 1995; Lozovatsky et al., 2006; Cisewski et al., 2008; Sutherland et al., 2014), and 10^{-5} m^2 s^{-1} using an ocean general circulation model (Noh and Lee, 2008). In this study, the XLD is specified as the depth where ε decreases from the first minimum value (e.g., 10^{-9} W kg^{-1} for A_o^b) (Table B1~~A2~~, Appendix B). This aligns with previous dissipation thresholds and ensures that dissipation~~mixing~~ is captured in midwater. Huang et al. (2019) showed that the H_{BBL} spatially varies between 15 and 123 m in the Atlantic Ocean, with a median of ~30-40 m in the North Atlantic. According to their findings, and based on bathymetry measurements and near-bottom current measurements from CTD-O_2/LADCP, we define the H_{BBL} in our study as 18 m for shallow stations and 40 m for deep stations.

2.2.2 Baroclinic currents

To analyze the processes explaining dissipation and mixing, particularly along IT paths, we estimate shear instabilities associated with the semi-diurnal (M_2) ITs and mean circulation, as well as their contributions to mixing.

The M2 tidal component of the tidal current is derived by calculating the baroclinic (semi-diurnal) tidal velocity $[u'', v'']$, following these equations:

$$[u', v'] = [u, v] - [u_{bt}, v_{bt}], \quad (1)$$

$$[u_{bt}, v_{bt}] = \frac{1}{H}\int_{-H}^{0} [u, v]dz, \quad (2)$$

$$[u'', v''] = [u', v'] - [\underline{u'}, \underline{v'}]. \quad (3)$$

Here, $[u, v]$ represent total horizontal (zonal u and meridional v) velocities obtained from SADCP data. The components $[u', v']$ and $[u_{bt}, v_{bt}]$ represent baroclinic and barotropic components of horizontal velocities, respectively . H is water depth. The baroclinic mean velocities $[\underline{u'}, \underline{v'}]$, calculated to estimate mean circulation along IT paths, are decomposed into along-shore $\underline{u'_l}$ and cross-shore $\underline{u'_c}$ velocities. The overbar denotes the average over the M_2 tidal period. Similarly, the components $[u'', v'']$ are decomposed into along-shelf u''_l and cross-shelf u''_c velocities. The along-shelf velocity component is defined parallel to the 200 m isobath (treated as the coastline), with positive values indicating northwestward flow and negative values indicating southeastward flow. The cross-shelf velocity component is defined perpendicular to the 200 m isobath, with positive values indicating northeastward flow and negative values indicating southwestward flow.

Note that continuously collected SADCP for some stations are not sufficiently resolved due to gaps filled by interpolating between time points. The similar processing is applied to the CTD-O_2 data. SADCP time series data are less than 17 hours at all long stations, except for S14, which spans 42 hours. As a result, the diurnal and semidiurnal period fittings are not formally distinct (except at A_{isw}), and the inertial period (at least 5 days) cannot be resolved in our dataset. This limits our ability to separate currents by frequency and examine the associated dissipation. The velocity profiles from LADCP are glued into our SADCP time series data below ~500 m depth at long stations.

To evaluate shear instabilities associated with ITs and the mean background circulation, we compute the baroclinic tidal vertical shear squared ($S^{2''}$) and mean shear squared ($\underline{S^{2'}}$) as follows:

$$S^{2''} = (\partial u''/\partial z)^2 + (\partial v''/\partial z)^2, \quad (4)$$

$$\underline{S^{2'}} = (\partial \underline{u'}/\partial z)^2 + (\partial \underline{v'}/\partial z)^2. \quad (5)$$

The individual contributions of semi-diurnal ITs and mean circulation are then expressed as follows: $S^{2''}/(\underline{S^{2'}} + S^{2''})$ for IT contribution and $\underline{S^{2'}}/(\underline{S^{2'}} + S^{2''})$ for mean circulation contribution. This calculation is used to quantify the contribution of tidal or mean shear during each dissipation event.

2.2.3 Ray-tracing calculation

Analyzing both the mean currents and the spatial dimension along the IT pathways offers another insight into the mechanisms responsible for observed mixing (Rainville and Pinkel, 2006). IT energy rays are generated in regions with steep topography, such as the shelf break, where the IT slope matches with the bottom slope (i.e., critical slopes) before propagating within the ocean interior. These rays, moving both downward and upward, encounter the seasonal pycnocline, resulting in beam scattering and the formation of large IT oscillations. As these oscillations steepen, they disintegrate into nonlinear ISWs, a process known as "local generation" of ISWs (New and Pingree, 1992). To explore IT paths, ray-tracing techniques are employed, as previously used by New and Da Silva (2002) and Muacho et al. (2014), to investigate the effectiveness and expected pathways of the IT beams off the Amazon shelf. One main assumption in our linear-theory-based hypothesis is that stratification remains horizontally uniform along the IT propagation path, although in reality, it may vary due to submesoscale and mesoscale variability. This limitation makes the ray tracing approach less realistic but still useful as a first-order estimate of energy distribution. The IT ray-tracing calculation assumes that in a continuously stratified fluid, IT's energy can be described by characteristic pathways of beams (or rays) with a slope c to the horizontal:

$$c = \pm\left(\frac{\sigma^2 - f^2}{N^2 - \sigma^2}\right)^{1/2}, \quad (6)$$

where σ is the M_2 tidal frequency (1.4052 x 10^{-4} rad s^{-1}), and f is the Coriolis parameter. Here, N^2 is the buoyancy frequency squared, which is calculated using the sorted potential density profiles (σ_θ). It is given by $N^2 = -(g/\rho_0)(d\sigma_\theta/dz)$, where ρ_0 is a reference density (1025 kg m^{-3}) and g is the gravitational acceleration. N^2 is obtained from time-averaged AMAZOMIX CTD-O_2 data, glued with monthly N^2 profiles from Amazon36 (NEMO model outputs, 2012-2016) below 1000 m depth. Amazon36

is a specific configuration, specifically designed to cover the western tropical Atlantic from the mouth of the Amazon River to the open sea (see Tchilibou et al., 2022; Assene et al., 2024; for configuration details and model description). The NEMO model's fine horizontal resolution (1/36°) and 75 vertical levels allow for accurate simulation of low-mode ITs generated along the Brazilian shelf break. Key inputs include bathymetric data from the 2020 General Bathymetric Chart of the Oceans, surface forcing from ERA-5 atmospheric reanalysis (Hersbach et al., 2020), and river runoff data from the ISBA (Interaction Sol-Biosphère-Atmosphère; https://www.umr-cnrm.fr/spip.php?article146&lang=en) model. Open boundary conditions were driven by 15 major tidal constituents (M2, S2, N2, K2, 2N2, MU2, NU2, L2, T2, K1, O1, Q1, P1, S1, and M4) and barotropic currents from the FES2014 atlas (Lyard et al., 2021), supplemented by temperature, salinity, and velocity data from the MERCATOR-GLORYS12v1 assimilation product (Lellouche et al., 2018).

Using N2 profiles from both Amazomix and Amazon36, IT ray-tracing diagrams are performed along the transects. The Upper (UTD) and Lower (LTD/LPD) Thermocline/Pycnocline Depth are delimited as defined by Assunçao et al. (2020). UTD corresponded to the depth where the vertical temperature gradient $\partial\theta/\partial z$ = 0.1 °C m^{-1}, while LTD/LPD were the last depths below the UTD at which $N^2 \geq 10^{-4}$ s^{-2}. Seasonal sensitivity tests of rays (August, September, October, and April) are conducted by varying the critical slope positions and N^2 to explore its influence and generate a set of ray paths consistent with characteristics of IT paths.

3 Results

3.1 Mixing

3.1.1 Thermohaline and IT features

In this subsection, we analyze density profiles (up-cast and down-cast) taken approximately six hours apart (half the M2 tidal period) along three transects (A^a, A^b, and E) defined on the HTE and LTE paths. Our aim is to examine the effects of mixing on water mass and the signatures of wave propagation.

First, mixing effects are evidenced in the step-like features of the density profiles (Fig. 4), indicating homogeneous layers. The vertical extent of these layers (L_{ρ_c}; Fig. 4b) is determined where the density gradient falls below the homogeneous threshold (0.01 kg m^{-3}) between 60–180 m depth, ranging from 4 to 41 m. These step-like features are more pronounced along the HTE transects (A^a and A^b), with examples including 10 m at A_s^a, 41 m at $A_{o_2}^a$, 13 m at $A_{o_3}^a$, and 20 m at A_{isw}, compared to the LTE transect E, where they are smaller (e.g., 4 m at E_s).

Second, wave propagation signatures are inferred from vertical displacements of isopycnals (constant density surfaces) between the two sampling times (Fig. 4c). Displacements range from 10 to 61 m across transects (Figs. 4a-4c). Along the 25 kg m^{-3} isopycnal, the largest shifts occur on the slope of transect A^a, with 40 m at A_s^a and 58 m at $A_{s_2}^b$, compared to 24 m at E_s on transect E. Displacements are smaller in the open ocean (e.g., 16 m at A_o^b and 15 m at $A_{o_1}^a$), except at A_{isw} (34 m) and $A_{o_3}^a$ (52 m). These displacements generally occur between 60–170 m depth, corresponding to the thermocline layer.

The presence of step-like structures and relevant vertical isopycnal displacements indicates strong shear-driven mixing in the mid-water column. These findings support the hypothesis of IT propagation, with higher amplitudes along the HTE paths (A^a and A^b) and lower amplitudes along the LTE transect E.

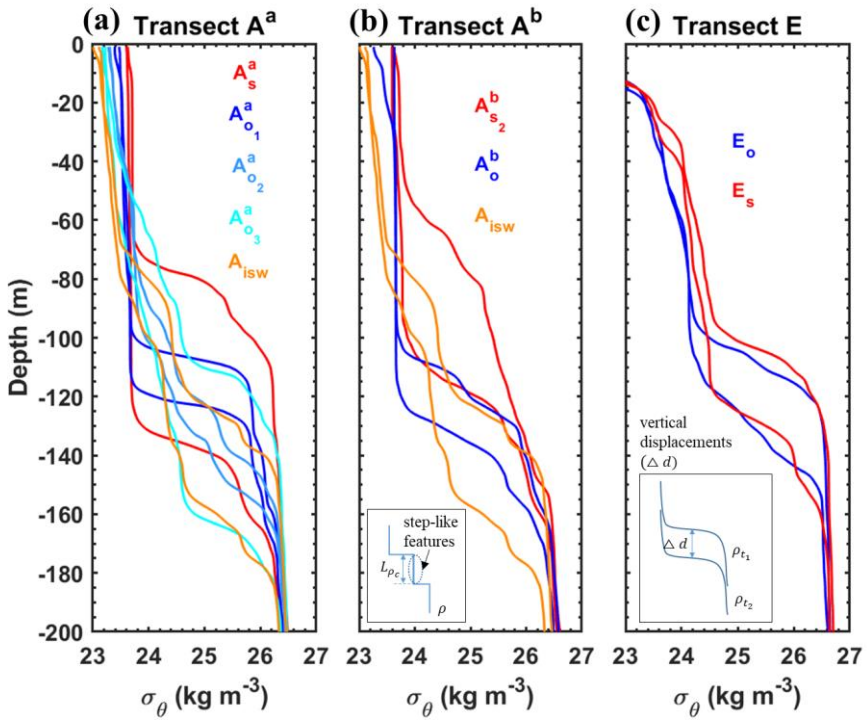

Figure 4: Density profiles (σ_θ, kg m^{-3}) from CTD-O_2 measurements during the AMAZOMIX 2021 cruise along transects: (a) A^a, (b) A^b, and (c) E. For long stations ($A^b_{s_2}$, A^b_o, A^a_s, $A^a_{o_1}$, $A^a_{o_2}$, $A^a_{o_3}$, A_{isw}, E_s, and E_o), two density profiles recorded ~6 hrs apart (half the M_2 tidal period) are shown to highlight step-like structures and vertical isopycnal displacements along the transects. Colored lines represent stations on the slope (red) and open ocean (blue, sky-blue, cyan, and light-orange). The subpanel in panel b depicts a step-like structure, where L_{ρ_c} represents the vertical extent of homogeneous regions and ρc denotes the density structure. The subpanel in panel c illustrates vertical displacements (Δd) of density structures, with ρ_{t_1} and ρ_{t_2} representing density structures at times t_1 and t_2, respectively.

3.1.2 TKE dissipation rates and mixing

Following subsection 2.2, the vertical distribution of dissipation rates (ε) was estimated to examine the effects of mixing on water masses along transects A^a, A^b, and E. Station-averaged ε values, ranging from [10^{-10}, 10^{-6}] W kg^{-1}, are presented in Figure 5.

Within the thermocline, the strongest ε values ([10^{-7}, 10^{-6}] W kg^{-1}) are measured at slope stations ($A^b_{s_1}$, $A^b_{s_2}$, and A^a_s) of the HTE transects, whereas lower values ([10^{-9}] W kg^{-1}) are recorded at station E_s (transect E). Elevated but relatively lower ε values ([10^{-8}] W kg^{-1}) are detected at open-ocean stations (e.g., A^b_o, $A^a_{o_2}$, and E_o) across all transects, except at station A_{isw}, where higher values ([10^{-7}] W kg^{-1}) are observed (Figs. 5a, 5c, and 5e).

Below the thermocline, elevated ε values ([10^{-8}] W kg^{-1}) persist at various depths at slope and open-ocean stations of the HTE transects (e.g., 375 m and 503 m for $A^b_{s_2}$; 390 m, 562 m, and 668 m for A^a_s; and 127 m and 192 m for A^b_o; Figs. 5a, 5c, and 5e), whereas on the LTE transect there is no evidence of such hotspots of dissipation~~mixing~~.

In the BBL, the highest ε values ([10^{-7}] W kg^{-1}) are found below 35 m depth at slope and shelf stations (A^b_{sh} and $A^b_{s_1}$) of transect A^b, while lower but still elevated values ([10^{-8}] W kg^{-1}) are observed at shelf stations of transects A^a and E (Figs. 5b, 5d, and 5f). Note that, at the base of MLD (between 15-30 m depth), elevated ε values (>10^{-7} W kg^{-1}) are found at slope stations A^a_s and $A^b_{s_2}$, and open-ocean stations $A^a_{o_2}$ and A_{isw} compared to other stations (Figs. 5a and 5c).

In summary, the vertical distribution of ε exhibits distinct spatial patterns across transects A^a, A^b, and E. Slope stations of the HTE transects A^a and A^b show higher values than those of the LTE transect E. Open-ocean stations generally display lower but still elevated values, except for station A_{isw}, which has higher ε. The HTE transects A^a and A^b consistently exhibit higher ε than the LTE transect E, which could emphasize the role of localized shear-driven mixing along IT paths, particularly in the open ocean. To further investigate the processes driving mixing, we analyze shear instability arising from current dynamics.

Formatted: Subscript

Formatted: Subscript

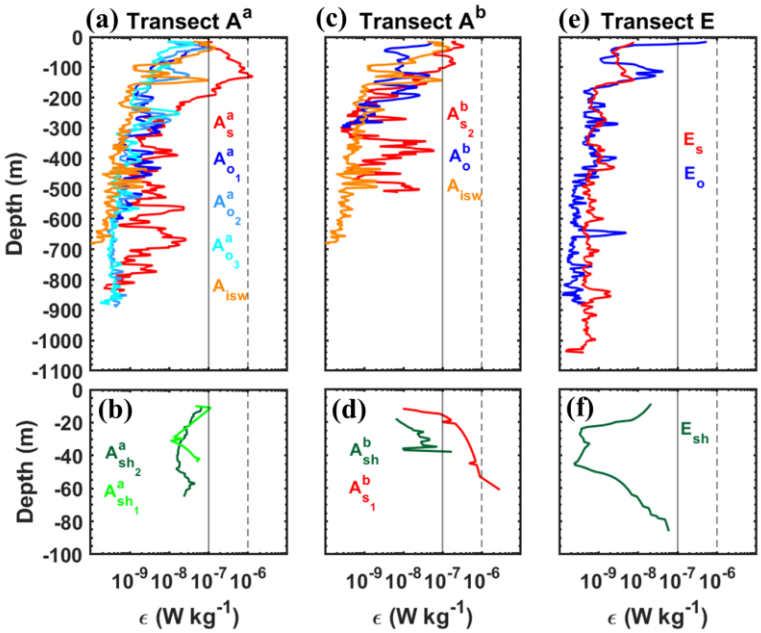

Figure 5: Station-averaged dissipation rate profiles (ε, in W kg^{-1}, logarithmic scale) from VMP measurements during the AMAZOMIX 2021 cruise along transects: (a)-(b) A^a, (c)-(d) A^b, and (e)-(f) E. Colored lines represent stations on the shelf (green, lime green), slope (red), and open ocean (blue, sky blue, cyan, and light orange). Vertical dashed and solid black lines are included for comparison.

3.2 Processes contributing to mixing

In this subsection, we focus on the midwater layer, and we investigate the processes that might be responsible for the high mixing activity described in the previous section. In particular, we analyze the vertical structure of baroclinic currents and separate the contributions of baroclinic tidal currents and time-averaged currents (in the following mean currents) to dissipation.

3.2.1 Mean baroclinic current

First, we focus on the mean baroclinic current. Following the method described in subsection 2.2.2 (Eqs. (1) and (5)), the vertical structure of the mean circulation is examined through the along-shelf components of the time-averaged (mean)

baroclinic velocities. Indeed, the along-shelf current is the dominant component of the mean circulation in the region, primarily driven by the NBC. Note that the analysis of cross-shelf components does not alter the results (figures not shown). For three contrasting long stations–two on the HTE transects (A_S^a and A_{isw}; Figs. 6a, 6b, and 8a) and one on the LTE transect (E_o; Figs. 7a, 7b, and 9a)–we show the vertical structure of the along-shelf mean baroclinic currents and the associated mean shear.

In the upper 200 m (referred to as the surface layer), a northwestward surface flow is observed at all stations except at E_s, where the flow direction is reversed to southeastward. Strong surface flow velocities (67-98 cm s-1; Table C1~~A3~~, Appendix C) are recorded at all stations south of 3°N (e.g., at A_{isw}; Fig. 6b), except at A_S^a, where velocities are reduced (~30 cm s^{-1}; Fig. 6a). Strong vertical shear ([1.1, 1.7] × 10^{-4} s^{-2}; Table C1~~A3~~, Appendix C) is observed at stations south of 3°N (e.g., at A_{isw}; Fig. 8b), except at A_S^a, where shear is weaker ([10^{-5}] s^{-2}; Fig. 8a) in the surface layer. At stations further north (above 4°N) in the surface layer, lower along-shelf velocities are noted for both northwestward (~43 cm s^{-1} at E_o; Fig. 7a) and southeastward flows (~28 cm s^{-1} at E_s; Table C1~~A3~~, Appendix C). Strong vertical shear (2.7 × 10^{-4} s^{-2} at E_o; Fig. 8a) is associated with the northwestward flow, while lower vertical shear ([10^{-5}] s^{-2} at E_s; Table C1~~A3~~, Appendix C) is observed for the southeastward flow. Below 200 m, a potential subsurface flow is identified between 200-700 m, particularly at stations south of 3°N (e.g., A_S^a; Fig. 6a), with weak vertical shear ([10^{-5}] s^{-2}; Fig. 8a).

These findings suggest that the mean background circulation may play a substantial role in driving mixing mechanisms off the Amazon shelf.

3.2.1 Baroclinic tidal current

Second, we focus on baroclinic tidal currents. Following the method described in subsection 2.2.2 (Eqs. (3) and (4)), we examined the vertical structure of tidal currents using the cross-shelf components of semi-diurnal baroclinic velocities. The cross-shelf current is likely the dominant component of IT currents in the region. Note that the along-shelf velocity components were weaker than the cross-shelf components (figures not shown). For the same three contrasting long stations, we present time-depth sections of cross-shelf baroclinic tidal currents (Figs. 6c, 6d, and 7b) and their associated tidal shear (Figs. 8c, 8d, and 9b).

On the slope at A_S^a, strong tidal current reversals occur approximately every six hours within the pycnocline (70-180 m depth; 24–26 kg m^{-3} isopycnals; Fig. 6c), corresponding to the M_2 tidal component. These reversals reach amplitudes of up to 45 cm s^{-1} (Fig. 6c) and vertically exhibit 6-7 alternating velocity peaks, indicating high vertical eigenmodes (modes 6-7; Fig. 6c). Similar conditions are observed at $A_{S_2}^b$, where tidal amplitudes reach 35 cm s^{-1} (Table C1~~A3~~, Appendix C) with eigenmodes 6-7. In contrast, reduced amplitudes (20 cm s^{-1}) and slightly lower eigenmodes (mode 4) are recorded at E_s. In the open ocean at E_o, tidal currents are weaker (up to 15 cm s^{-1}; Fig. 7b) with eigenmodes around mode 4. Other open-ocean stations ($A_{O_1}^a$, $A_{O_3}^a$, and A_O^b) show weak tidal amplitudes (15-25 cm s^{-1}; Table C1~~A3~~, Appendix C) and lower eigenmodes (modes 3-5). However,

exceptions are noted at A_{isw} and $A_{o_2}^a$, where amplitudes remain high (40 cm s^{-1}; Table C1~~A3~~, Appendix C), particularly near the pycnocline.

On the slope, tidal vertical shear ranges between [1.2, 7.7] × 10^{-4} s^{-2}. The strongest shear (7.7 × 10^{-4} s^{-2}; Fig. 8c) occurs at A_s^a within the pycnocline, while the weakest (1.2 × 10^{-4} s^{-2}; Table C1~~A3~~, Appendix C) is at E_s. In the open ocean, shear varies between [2.0, 7.6] × 10^{-4} s^{-2} (Table C1~~A3~~, Appendix C), with lower values (3.5 × 10^{-4} s^{-2}; Fig. 9b) at E_o. Exceptions again occur at A_{isw} and $A_{o_2}^a$, where baroclinic tidal shear remains relatively strong (between [5.0, 7.6] × 10^{-4} s^{-2}; Fig. 8d; Table C1~~A3~~, Appendix C), particularly near the pycnocline.

Along the slope, baroclinic tidal currents and shear are stronger along the HTE transects compared to LTE. In the open ocean, they are generally weaker, except at A_{isw} and $A_{o_2}^a$, where they remain high. These tidal currents and their associated shear coincide with strong vertical displacements of N^2 maxima (subsection 3.1.1) and high dissipation rates (subsection 3.1.2), raising the question of whether high mixing activity is primarily driven by IT or mean currents.

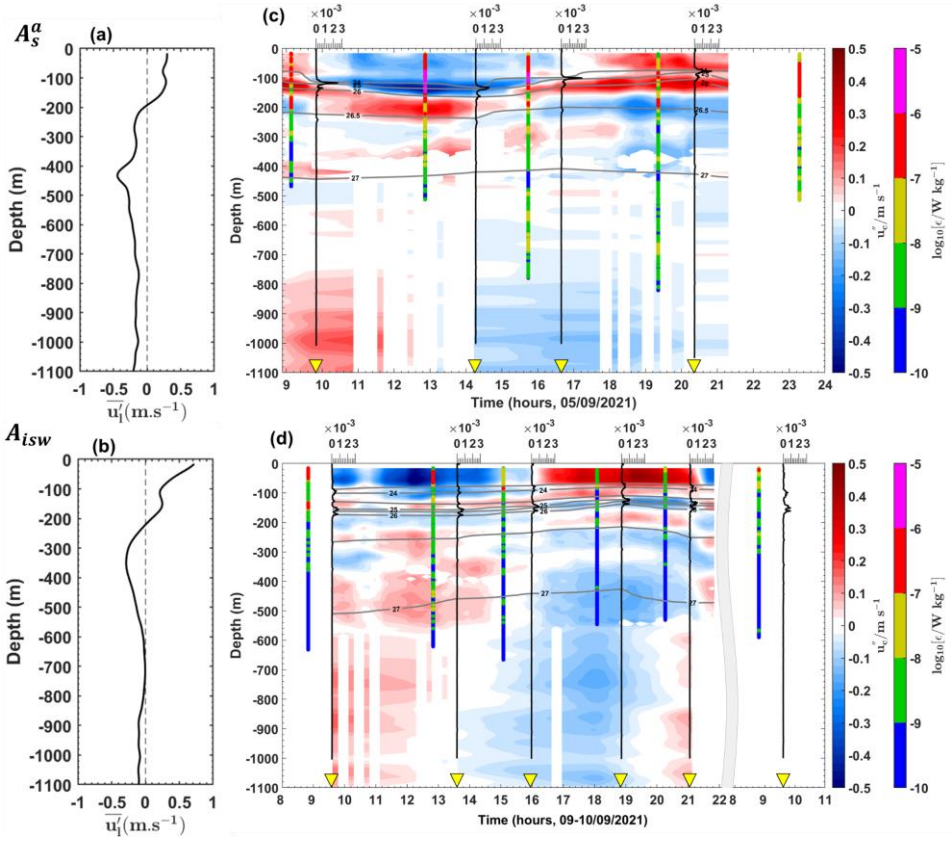

Figure 6: (a)-(b) Along-shelf mean baroclinic currents ($\underline{u'}_l$, in m s^{-1}) and (c)-(d) cross-shelf semi-diurnal baroclinic currents (u''_c, in m s^{-1}) from the ADCP for stations (a)-(c) A_s^a and (b)-(d) A_{isw}. Panels (c) and (d) also show the buoyancy frequency squared (N^2, in s^{-2}) as vertical black lines, potential density (σ_θ, kg m^{-3}) as grey contours, and dissipation rate profiles (ε, in W kg^{-1}, logarithmic scale) as vertical colored bars.

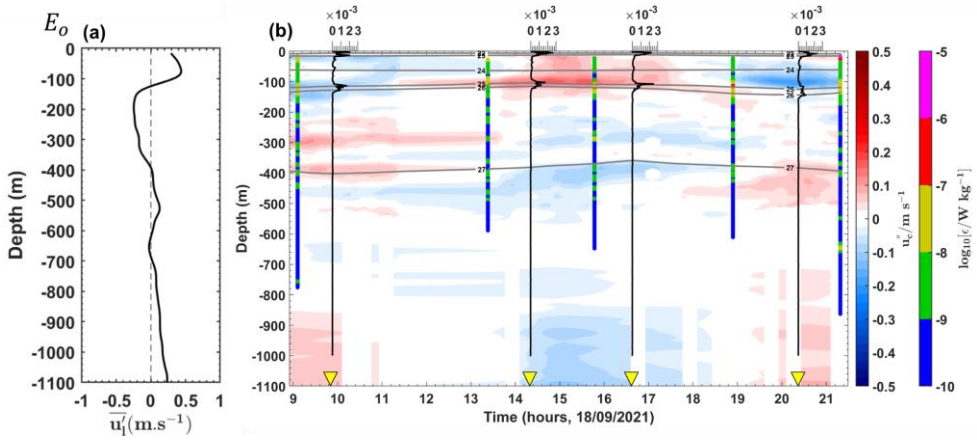

Figure 7: Panels follow the same format as in Figure 6 but correspond to station E_o.

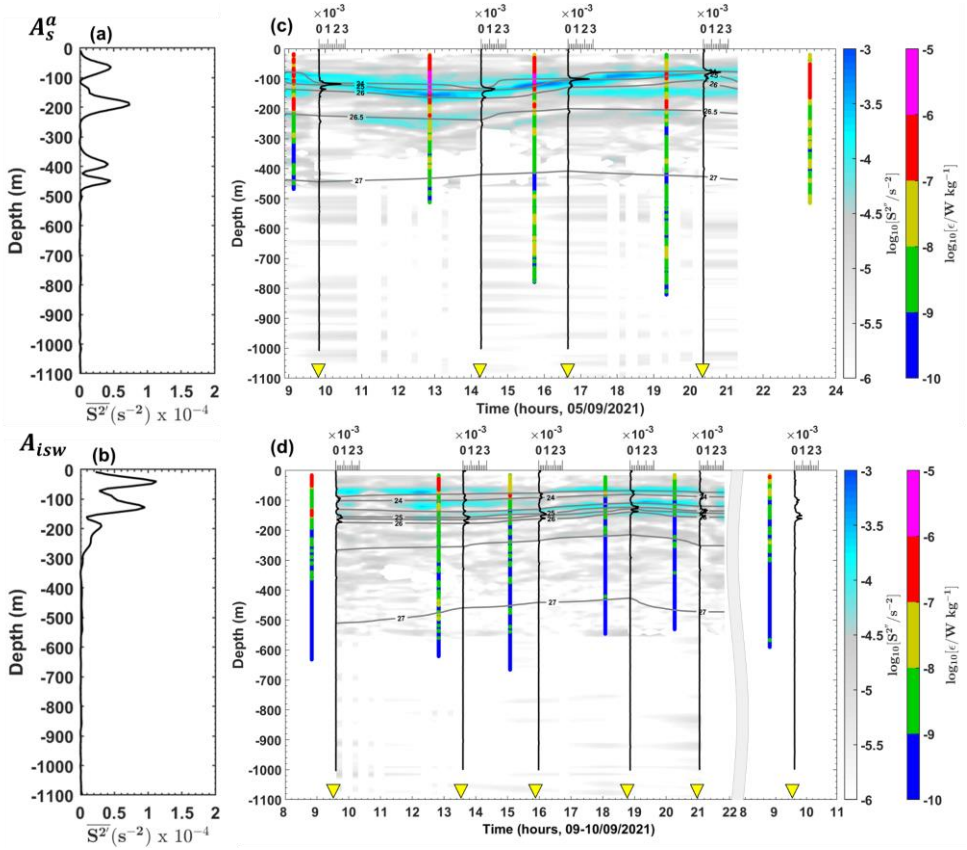

Figure 8: (a)-(b) Mean baroclinic vertical shear squared ($\underline{S^{2\prime}}$, in s^{-2}) and (c)-(d) semi-diurnal baroclinic vertical shear squared ($S^{2''}$, in s^{-2}, logarithmic scale) from the ADCP for stations (a)-(c) A_s^a and (b)-(d) A_{isw}. Panels (c) and (d) also show the buoyancy frequency squared (N^2, in s^{-2}) as vertical black lines, potential density (σ_θ, kg m^{-3}) as grey contours, and dissipation rate profiles (ϵ, in W kg^{-1}, logarithmic scale) as vertical colored bars.

Formatted: Subscript

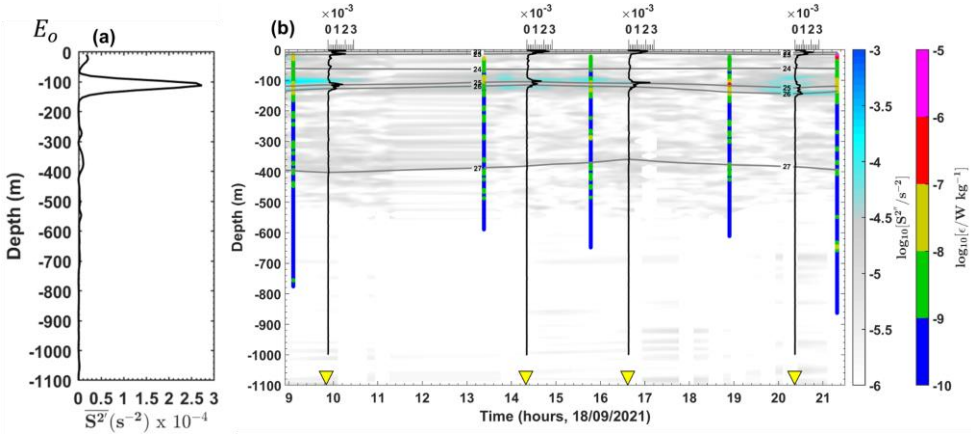

Figure 9: Panels follow the same format as in Figure 8 but correspond to station E_o.

3.2.3 Competitive processes to generate mixing

Our aim in this subsection is to associate midwater mixing events with either baroclinic tidal currents or time-averaged (mean) currents. To achieve this, we map depth-integrated and maximum values of station-averaged ε and plot all ε values on a (time-mean shear $S^{2\prime}$, tidal shear $S^{2''}$) diagram across five regions (A_s, A_o, A_{isw}, E_s, and E_o; Figs. 10 and 11). These regions are selected to contrast slope and open-ocean dynamics, with data included from the HTE and LTE transects. All data are collected from below the wind-influenced surface layer (defined as the maximum of XLD or MLD; see subsection 2.2.1) and above the friction-dominated bottom boundary layer (H_{BBL}; defined in subsection 2.2.1). Following the approach described in subsection 2.2.2, we calculated the relative contributions (%) of tidal shear and mean shear to the total baroclinic shear in order to quantify their role during each mixing event.

Dissipation~~Mixing~~ hotspots (ε = [10^{-6}, 10^{-7}] W kg^{-1}; magenta and red circles in Fig. 11 and Fig. 10) are observed under strong vertical baroclinic shear ([10^{-4}, 10^{-5}] s^{-2}), driven by either tidal or time-mean currents.

On the slope (A_s and E_s), high ε values in A_s are associated with stronger $S^{2''}$ than $S^{2\prime}$ (magenta, red, and grey stars in Fig. 11a correspond to $S^{2''} \approx 10^{-4} > S^{2\prime} \approx 10^{-5}$), indicating that tidal shear contributes~~explains~~ ~60% to~~of~~ high ε values (Table B1~~A3~~, Appendix B~~C~~). Similarly, in E_s, moderate ε values (yellow and grey stars in Fig. 11d) are primarily driven by tidal shear, which accounts for ~60% of the observed dissipation~~mixing~~ (Table B1~~A3~~, Appendix B~~C~~).

In the open ocean (A_o, E_o, and A_{isw}), moderate ε values in A_o and E_o are found when $S^{2''}$ is nearly equal to $S^{2\prime}$ (yellow, red, and grey stars in Fig. 11b and 11e correspond to $S^{2''} \approx S^{2\prime} \approx 10^{-4}$ s^{-2}), suggesting tidal and time-mean shear each contribute

Formatted: Subscript
Formatted: Subscript
Formatted: Superscript

~50% to dissipation~~mixing~~ (Table B1~~A3~~, Appendix B~~C~~). An exception is observed in A_{isw}, where high ε values coincide with slightly stronger tidal shear (red and grey stars in Fig. 11c correspond to $S^{2''} \approx 2 \times \underline{S^{2'}} \approx 2 \times 10^{-4}$ s^{-2}), suggesting that tidal shear contributes~~explains~~ ~60 % to~~of~~ dissipation~~mixing~~ hotspots (Table B1~~A3~~, Appendix B~~C~~).

These results suggest that dissipation~~mixing~~ on the slope is slightly dominated by ITs, while offshore dissipation~~mixing~~ is equally balanced by mean circulation and ITs. However, exceptions exist in the open ocean, particularly at stations A_{isw} and A_o^b, where tidal shear contributes ~60% and ~30% to dissipation~~mixing~~, respectively. The dissipation~~mixing~~ at A_o^b is attributed to NBC. A key question remains: why does A_{isw} exhibit strong IT-driven dissipation~~mixing~~ ~230 km from IT generation sites, with dissipation~~mixing~~ hotspots observed at various depths throughout the water column? To address this, we employ ray-tracing techniques to investigate potential IT propagation paths.

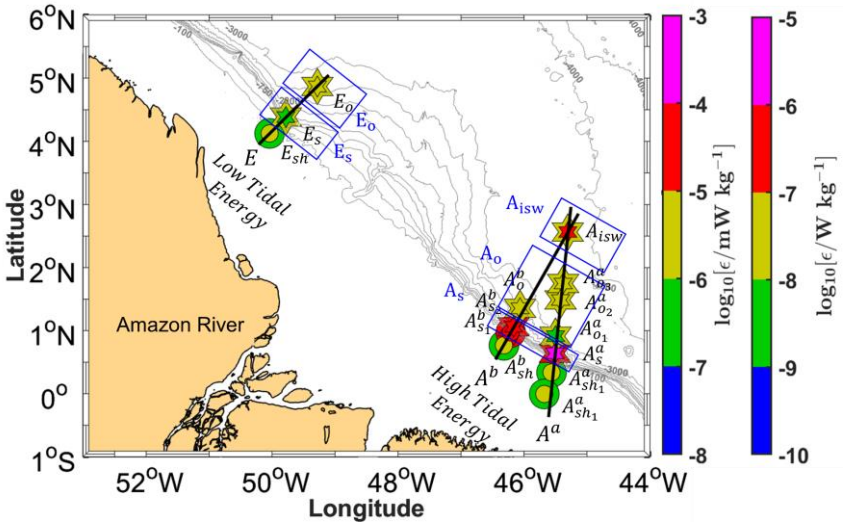

Figure 10: Depth-integrated (in mW kg^{-1}, logarithmic scale) and maximum values (in W kg^{-1}, logarithmic scale) of station-averaged dissipation rates (ε) from VMP measurements during the AMAZOMIX 2021 cruise. Solid black lines depict transects (A^a, A^b, and E) along high tidal energy (HTE) and low tidal energy (LTE) paths. Data are from below the wind-influenced surface layer and above the friction-dominated bottom boundary layer. Colored circles and stars represent short and long stations, respectively. Small and large colored circles indicate depth-integrated and maximum values of ε, respectively, with ranges shown by the color bar. Similarly, small and large colored stars indicate depth-integrated and maximum values of ε, respectively, with ranges shown by the color bar. Stations are grouped into five areas: A_s (A_s^a and $A_{s_2}^b$), A_o (A_o^b, $A_{o_1}^a$, $A_{o_2}^a$, and

$A^a_{o_3}$), A_{isw} (A_{isw}), E_s (E_s), and E_o (E_o). *The five blue boxes indicate these defined areas. Subscripts denote locations: "s" for slope (A_s), "o" for offshore (A_o and E_o), and "isw" for ISW regions (A_{isw}).*

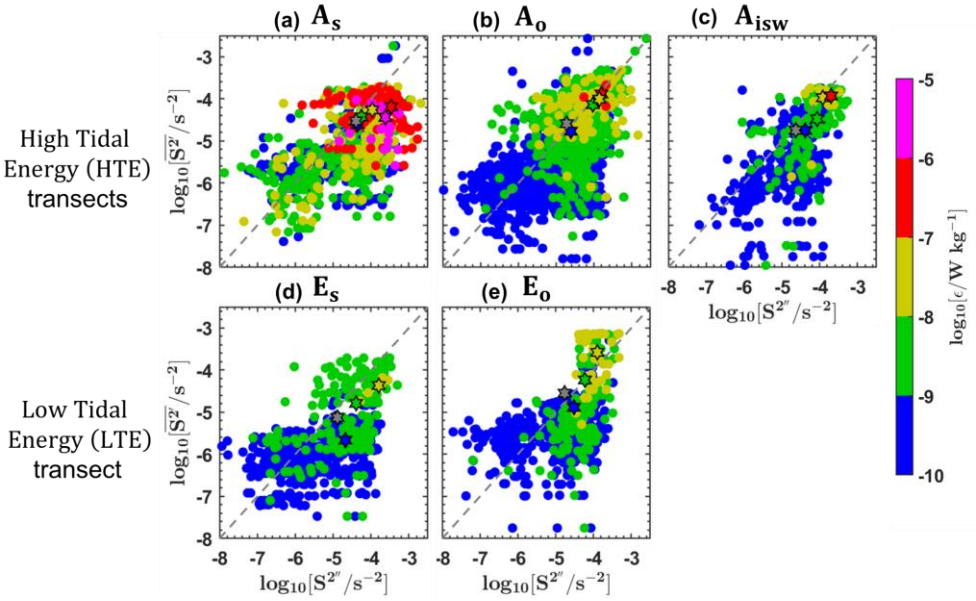

Figure 11: Dissipation rates (ε, in W kg^{-1}, logarithmic scale), measured below the wind-influenced surface layer (max [XLD, MLD]) and above the friction-dominated BBL (H_{BBL}), plotted as a function of the mean baroclinic vertical shear squared ($S^{2'}$, in s^{-2}, logarithmic scale) and semi-diurnal baroclinic vertical shear squared ($S^{2''}$, in s^{-2}, logarithmic scale). Data are from defined areas: (a) A_s (A^a_s and $A^b_{s_2}$), (b) A_o (A^b_o, $A^a_{o_1}$, $A^a_{o_2}$, and $A^a_{o_3}$), (c) A_{isw} (A_{isw}), (d) E_s (E_s), and (e) E_o (E_o). ε are represented by colored circles, with their ranges indicated on the color bar. Each panel also includes vertical shear averages for specific ε ranges ([10^{-6}], [10^{-7}], [10^{-8}], [10^{-9}], and [10^{-10}] W kg^{-1}), depicted as colored stars with black edges, grey stars with black edges represents the vertical shear averaged across all ε values. Dashed grey lines are included for comparison.

Formatted: Superscript

3.2.4 IT ray-tracing

In this subsection, IT ray paths are computed for the M_2 tidal frequency, following the method described in subsection 2.2.3 (Eqs. (6)). These computations provide insights into linear theoretical energy flux paths in the vertical dimension (Rainville

and Pinkel, 2006). The results will be compared to previously estimated dissipation rates to explain the intense dissipation~~mixing~~ hotspot observed at A_{isw}, which contrasts with values typically found in the open ocean (Gille et al., 2012). Figures 12 and 13 show that linear IT rays, derived from both model and observed density data, are generated at the critical slope near the 93 m and 121 m isobaths on the HTE and LTE transects, respectively. After generation, the rays propagate downward through the water column, reflect at the seabed, and then propagate upward, where they are expected to reflect at the surface. This pattern continues seaward (Figs. 12 and 13). In reality, part of the IT beam may also reflect within the pycnocline. Surface reflections are observed at large distances from the ray generation sites: ~105 km and ~230 km on transect A^a (Fig. 12a) and ~100 km and ~220 km on transect A^b (Fig. 12b). These large distances may result from the greater orientation angle between the IT propagation direction and the transects. In contrast, surface reflections on transect E occur at shorter distances (~80 km and ~205 km; Fig. 13), possibly due to eddy activity (Dossa et al., in preparation). The linear rays suggest horizontal wavelengths of ~90-125 km, consistent with mode-1 IT. Differences between transects may arise from variations in density, ocean depth, or the angle between the IT propagation path and the transect orientation. The curvature of the rays becomes more pronounced as they interact with the pycnocline, particularly between 20-207 m depth, defined by the upper and lower thermocline depths (UTD and LTD; Figs. 12 and 13).

Tracking the IT rays along the transects reveals their possible alignment with dissipation~~mixing~~ hotspots (Figs. 12 and 13). On the slope, dissipation~~mixing~~ hotspots (between 60-180 m depth; Fig. 12a-b) at A_s^a and $A_{s_2}^b$ and around 15 km at the surface bounce likely result from nonlinear processes involving high-mode IT—such as IT breaking and shear instabilities—that are not captured by linear ray theory.~~from their proximity to the ray generation sites~~. In the open ocean, the surface dissipation~~mixing~~ (at 34 m depth; Fig. 12a) at $A_{o_2}^a$ may arise from surface reflections of the rays. Meanwhile, dissipation~~mixing~~ hotspots between 130–152 m depth at A_{isw} could result from either ray interference creating instabilities at multiple depths or the arrival of rays from transect A^a (at 87 m and 150 m depth; Fig. 12a) and transect A^b (at 275 and 523 m depth; Fig. 12b) at A_{isw}.

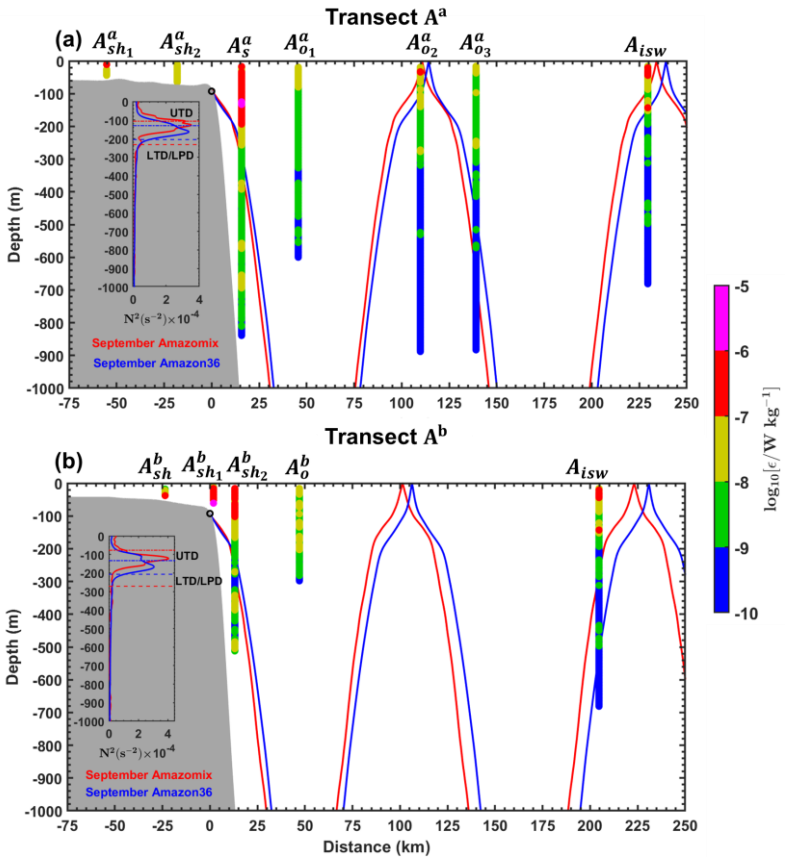

Figure 12: Ray-tracing diagrams for M_2 constituent of IT along transects (a) A^a and (b) A^b. Ray calculations were performed using the mean buoyancy frequency squared (N^2, in s^{-2}) derived from CTD-O_2 data (red ray) and NEMO-Amazon36 model data (blue ray) for September. Grey areas represent local topography, and black circles indicate the critical topography slopes (ray generation sites). Subpanels show N^2 profiles from AMAZOMIX (red line) and the NEMO-Amazon36 model (blue line), used for ray-tracing calculations. Upper Thermocline Depth (UTD, dotted lines) and Lower Thermocline/Pycnocline Depth (LTD/LPD, dashed lines) are also indicated in the subpanels.

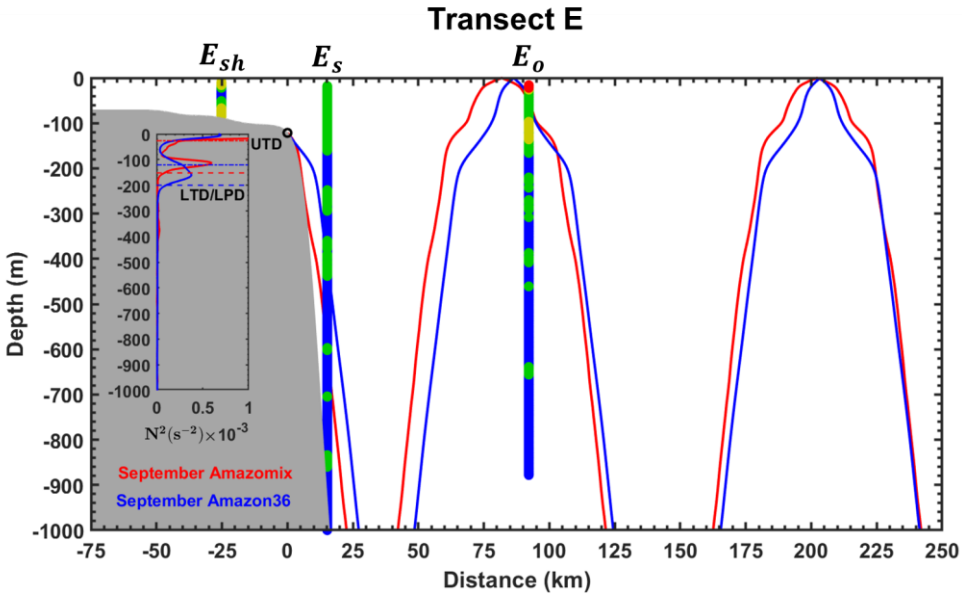

Figure 13: Panels follow the same format as in Figure 12 but correspond to transect E.

4 Discussion and Conclusion

The AMAZOMIX 2021 cruise provided, to the best of our knowledge, for the first time, direct measurements of turbulent dissipation using a VMP at multiple stations along contrasting IT paths. These measurements enabled the study of mixing processes at the Amazon Shelf break and the adjacent open ocean. To capture a full tidal cycle, data on turbulent dissipation rates, hydrography, and currents were collected alternately over 12 hours, with 4 to 5 profiles taken per station (see section 2). The locations of the 12-hour sampling stations were selected based on modeling results that provided realistic maps of IT generation, propagation and dissipation (Fig. 1; Tchilibou et al., 2022). Stations were located along the HTE paths A^a and A^b ($A^a_{sh_1}$ $A^a_{sh_2}$, A^a_s, $A^a_{o_1}$, $A^a_{o_2}$, $A^a_{o_3}$, A_{isw}, A^b_{sh}, $A^b_{s_1}$, $A^b_{s_2}$, and A^b_o) and LTE path E (E_{sh}, E_s, and E_o).

Vertical displacements, homogeneous layers

First, step-like features were found in the density profile that characterized homogenized layers stacked atop one another, indicating intense mixing hotspots at various depths in the water column. Their vertical extent ranged between 4 and 41, consistent with step-like structures observed in other IT regions (Koch-Larrouy et al., 2015; Bouruet-Aubertot et al., 2018).

Our results show that along the HTE paths (A^a and A^b), step-like structures were larger in the open ocean (up to 41 m) than over the (up to 10 m). In contrast, along the LTE path (E), they were smaller (4 m) and uniform across both the slope and open ocean, indicating weaker mixing.

Second, vertical isopycnal displacements ranged from 10 to 61 m, aligning with observations from other IT regions (Stansfield et al., 2001; Simpson and Sharples, 2012; Bordois, 2015; Koch-Larrouy et al., 2015; Zhao et al., 2016; Bouruet-Aubertot et al., 2018; Xu et al., 2020) that show similar order of magnitude. On the HTE paths, the strongest displacements occurred over the slope (up to 58 m), with substantial variability in the open ocean (15–52 m). On the LTE path, displacements were weaker (24 m) and confined to the slope.

The differences between the open ocean and slope, as well as between HTE and LTE paths, are seemingly associated with IT propagation, which induces vertical displacements at tidal frequencies, promoting mixing and forming the step-like density features observed.

Direct measurements of dissipation rates

The station-averaged dissipation rate (ε) ranged from 10^{-10} to 10^{-6} W kg^{-1}, with distinct spatial patterns across paths A^a, A^b, and E. The highest ε values (10^{-7} to 10^{-6} W kg^{-1}) were observed at slope stations of the HTE paths, while lower ε values (10^{-9} W kg^{-1}) were found at slope stations of the LTE path (Figure 14). Open ocean ε values were generally lower (10^{-8} W kg^{-1}) but still elevated, especially at A_{isw}, where values reached 10^{-7} W kg^{-1} near the pycnocline. The elevated ε near slopes on the HTE paths aligns with observations from other energetic IT generation sites (e.g., the Hawaiian Ridge, Klymak et al., 2008; Halmahera Sea, Koch-Larrouy et al., 2015; Bouruet-Aubertot et al., 2018). In contrast, lower ε values near slopes on the LTE path are comparable to those in less energetic IT regions (e.g., Takahashi and Hibiya, 2019). In the open ocean, ε values–though lower than slope measurements–remain elevated, particularly at A_{isw}, where they exceed typical background levels (10^{-10}-10^{-8} W kg^{-1}; e.g., Southern Ocean, Gille et al., 2012; Banda Sea, Bouruet-Aubertot et al., 2018). This suggests localized turbulent dissipation~~mixing~~, likely driven by ITs or mesoscale currents.

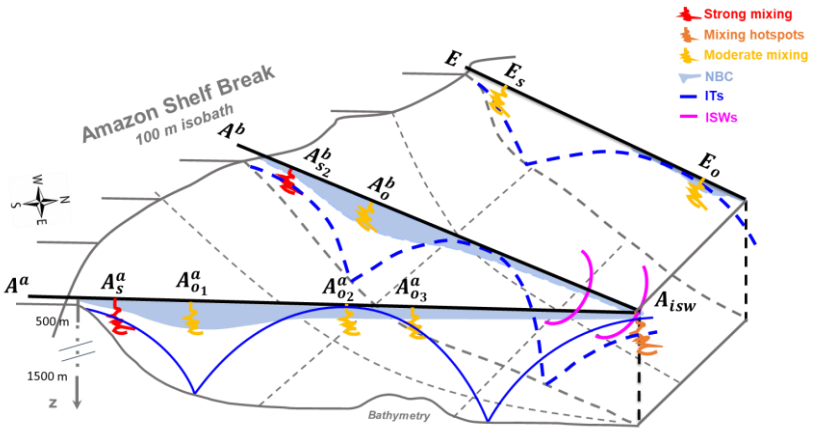

Figure 14: Summary diagram illustrating the key processes driving mixing across the HTE paths (A^a and A^b) and LTE path (E) off the Amazon shelf. At IT generation sites (stations A^a_s, $A^b_{s_2}$, and E_s), mixing is generally stronger (red zigzags), except at E_s, where it is moderated (yellow zigzags). At these generation sites, ITs contribute ~60% ~~to of the~~ mixing, exceeding the contribution of the mean circulation (NBC). Away from generation sites in the open ocean (e.g., A^b_o, $A^a_{o_1}$, and E_o; yellow zigzags), mixing decreases but remains substantial, driven by nearly equal contributions from ITs and mean circulation. A key observation is the increased mixing ~230 km from the generation sites, forming a hotspot at A_{isw} (orange zigzags). This coincides with the surfacing of IT rays (blue lines) from two distinct generation sites on the HTE paths, the vanishing of the NBC (sky blue shaded areas), and the presence of ISWs (magenta lines). These observations suggest that constructive interference of IT rays may generate ISWs, amplifying mixing at A_{isw}.

Enhanced dissipation~~mixing~~ at the base of the MLD

Near the base of the MLD (15-30 m depth), high ε values (>10^{-7} W kg^{-1}) were observed at slope stations (A^a_s and $A^b_{s_2}$) and open-ocean stations ($A^a_{o_2}$ and A_{isw}) along the HTE paths. These findings agree with model results from Tchilibou et al. (2022) and Assene et al. (2024), which identified similar near-surface ε hotspots in the HTE regions.

Contribution of background circulation and ITs to mixing

To identify the processes driving the observed high mixing activity, we analyzed shear instabilities in both mean and semi-diurnal baroclinic currents and quantified their relative ~~mixing~~ contributions to mixing.

Mean baroclinic current shear

First, we analyzed the along-shelf component of the mean baroclinic current (MBC), as it dominates the mean circulation in the region. MBC was primarily observed in the surface layer (0-200 m depth), driven by a northwestward flow with strong velocities (67-98 cm s^{-1}) and shear instability (between [1.1, 1.7] × 10^{-4} s^{-2}) at all stations south of 3°N. This flow is associated with the NBC, which moves northwestward along the Brazilian coast (Johns et al., 1998; Bourlès et al., 1999). However, at slope station A_s^a, NBC velocities were lower (~30 cm s^{-1}) with weak NBC vertical shear (~10^{-5} s^{-2}), likely due to topographic effects that weaken NBC near the continental slope (Silveira et al., 1994). Further north (above 4°N), the surface layer exhibited weak MBC with low shear instability (~10^{-5} s^{-2}) in the open ocean, except near the slope, where MBC reversed to southeastward with strong shear (2.7 × 10^{-4} s^{-2}). This reversal could be related to subsurface eddy activity (Dossa et al., in preparation) and the retroflection of the NBC, both common features in the region (Fratantoni et al., 2008). Below the surface layer (200-700 m depth), a potential southeastward flow beneath the NBC was observed, with weak shear instability (~10^{-5} s^{-2}), particularly near the slope south of 3°N (e.g., at A_s^a). This flow may be associated with a subsurface countercurrent (Dossa et al., in preparation).

IT shear

Second, the semi-diurnal (M_2) baroclinic currents were extracted from the total baroclinic current, revealing pronounced IT signatures and associated tidal shear on the slope compared to the open ocean. Tidal amplitudes, eigenmodes, and shear were stronger along the HTE paths compared to the LTE path. At slope stations on the HTE paths, tidal amplitudes were high (35-45 cm s^{-1}) with dominant modes 6-7, whereas at slope stations on the LTE path, amplitudes were reduced (20 cm s^{-1}) with mode 4. In the open ocean, tidal amplitudes and modes were generally lower (15-25 cm s^{-1}; modes 3-5), except at A_{isw} and $A_{o_2}^a$, where amplitudes remained elevated (40 cm s^{-1}), particularly near the pycnocline. Vertical shear associated with baroclinic tidal currents was also stronger along the HTE paths, with values of 5.5-7.7 × 10^{-4} s^{-2} at slope stations, compared to 1.2 × 10^{-4} s^{-2} along the LTE path. In the open ocean, shear values were generally weaker (2.0–3.5 × 10^{-4} s^{-2}), except at A_{isw} and $A_{o_2}^a$, where they remained high (5.0–7.6 × 10^{-4} s^{-2}), particularly around the pycnocline. Strong IT signals–observed in amplitudes, modes, and associated shear–near slopes along the HTE paths align with measurements at other generation sites (e.g., Hawaiian Ridge, Zhao et al., 2016; Ombai Strait and Halmahera Sea, Bouruet-Aubertot et al., 2018). In contrast, slightly weaker IT signals near slopes along the LTE path are consistent with observations from regions of low IT activity (e.g., Banda Sea, Bouruet-Aubertot et al., 2018). Offshore, IT signals are typically weak, consistent with areas distant from generation sites (e.g., Halmahera Sea, Bouruet-Aubertot et al., 2018), except at stations A_{isw} and $A_{o_2}^a$, where there are IT signal hotspots.

These results suggest that shear instabilities–driven by the mean flow and IT–may lead to mixing off the Amazon shelf, raising the question of whether MBC or IT dominates the mixing process.

IT/MBC ratio

Through direct quantification, we determined the relative contributions of MBC and IT to mixing. The results showed that both IT and MBC shear contribute to mixing, with their relative dominance varying across the HTE paths and LTE path. Near generation sites at slope stations (A_s^a, $A_{s_2}^b$, and E_s), IT shear dominated the IT/MBC shear ratio, contributing approximately ~60% to mixing. At open-ocean stations farther from generation sites (e.g., at $A_{o_2}^a$, $A_{o_3}^a$, and E_o), the contributions were nearly balanced, with each contributing around 50%. Exceptions in the open ocean were observed at station A_{isw}, where IT shear became dominant again (contributing ~60%), and at station A_o^b, where IT shear contribution decreased to ~30%. These results show that strong mixing near IT generation sites is primarily driven by IT shear instability, coherent with other sites (Klymak et al., 2008; Koch-Larrouy et al., 2015; Bouruet-Aubertot et al., 2018). Offshore, weaker mixing along IT paths is due to both IT and mean flow shear instability. This reduced mixing could result from ITs interacting with background flows, which advect energy away, or from effective offshore radiation (Whalen et al., 2012). At A_o^b, away from generation sites, the lower IT shear contribution to mixing was attributed to the strong influence of the MBC, dominated by the NBC.

The most relevant finding of this study was an increased mixing near the pycnocline layer, which surfaces at A_{isw} in the open ocean. This supports the results of Assene et al. (2024) and Macedo et al. (submitted).

Unexpected strong open-ocean dissipation~~mixing~~ at A_{isw}

Along the HTE paths at station A_{isw}, elevated remote dissipation rates (~10^{-7} W kg^{-1}) were detected ~230 km from the shelf break. This region has been modeled as a surface-reaching IT dissipation hotspot (Tchilibou et al., 2022; Assene et al., 2024), driving sea surface temperature cooling (Assene et al., 2024). Observations also link this area to chlorophyll blooms (de Macedo et al., submitted; M'Hamdi et al., in preparation) and the generation of large-amplitude (>100 m) nonlinear IT-induced (Brandt et al., 2002; de Macedo et al., 2023).

Our key findings quantify dissipation~~mixing~~ hotspots in the water column at A_{isw}, including intensified dissipation~~mixing~~ at the mixed-layer base, providing in situ validation for prior model hypotheses (Tchilibou et al., 2022; Assene et al., 2024). We further propose that IT disintegration into nonlinear, more dissipative baroclinic flux may occur here. At A_{isw}, IT rays from two distinct generation sites (A^a and A^b) surface alongside documented ISWs, coinciding with the vanishing point of NBC. This interaction zone may foster constructive interference of IT rays, potentially creating higher tidal modes (New & Pingree, 1992; Silva et al., 2015; Barbot et al., 2021; Solano et al., 2023). Such modes could enhance nonlinear ISW generation (e.g., Jackson et al., 2012) and explain the observed elevated dissipation rates (Xie et al., 2013).

Appendix A

The AMAZOMIX measurement sites and stations were systematically named and organized by location. Each site received a unique identifier based on its position along the HTE and LTE paths. Stations were categorized by site and region: superscripts "a" and "b" denoted stations at sites A^a and A^b, respectively, while subscripts indicated location–"sh" for shelf, "s" for slope,

"o" for offshore/open ocean, and "isw" for ISW regions (Table A1). This structured naming system ensured clear identification and logical grouping of stations for consistent data analysis.

Table A1: *The naming system of the AMAZOMIX cruise measurement sites and stations.*

Paths / Transects	Sites	Stations							
		Shelf		Slope		Offshore/Open ocean			ISWs
High Tidal Energy (HTE) paths	A^a	$A^a_{sh_1}$	$A^a_{sh_2}$	A^a_s		$A^a_{o_1}$	$A^a_{o_2}$	$A^a_{o_3}$	A_{isw}
	A^b	A^b_{sh}		$A^b_{s_1}$	$A^b_{s_2}$	A^b_o			
Low Tidal Energy (LTE) path	E	E_{sh}		E_s		E_o			-

Appendix B

To relate each mixing event with either tidal or mean (time-averaged) currents along the HTE transects (A^a and A^b) and the LTE transect (E), we quantify the relative contributions of mean and semi-diurnal baroclinic vertical shear squared at transect stations (see Table B1~~A2~~).

Table B1A2: *miXing Layer Depth (XLD), Mixed Layer Depth (MLD), Contribution (mean and standard deviation) of the Semi-diurnal (CSBS), and Mean Baroclinic (CMBS) Shear to total baroclinic shear.*

Stations	XLD (m)	MLD (m)	CSBS (mean ± SD) (%)	CMBS (mean ± SD) (%)
A_{sh}^{b}	27	25.0	-	-
$A_{s_1}^{b}$	20	5.0	-	-
$A_{s_2}^{b}$	57	17.8	66.2 ± 0.3	33.8 ± 0.3
A_{o}^{b}	46	22.5	36.7 ± 3.7	63.3 ± 3.7
$A_{sh_2}^{a}$	23	44.5	-	-
$A_{sh_1}^{a}$	29	21.0	-	-
A_{s}^{a}	26	32.5	60.0 ± 4.0	40.0 ± 4.0
$A_{o_1}^{a}$	104	15.5	47.6 ± 4.9	52.4 ± 4.9
$A_{o_2}^{a}$	75	11.3	56.6 ± 3.3	43.4 ± 3.3
$A_{o_3}^{a}$	82	12.3	59.1 ± 3.4	40.9 ± 3.4
A_{isw}	97	12.3	63.6 ± 4.8	36.4 ± 4.8
E_{sh}	45	1.0	-	-
E_{o}	73	1.8	56.6 ± 3.9	43.4 ± 3.9
E_{s}	53	1.0	60.2 ± 2.8	39.8 ± 2.8

SD = Standard Deviation.

Formatted: Font: Bold

Appendix C

Following subsection 2.2.2, we examined the cross-shelf component of baroclinic tidal currents to investigate IT amplitude (current strength) and shear instability around the pycnocline (70–180 m depth; see Table C1A3). Additionally, the along-shelf component of mean baroclinic currents (MBC) was analyzed to evaluate the strength of the mean flow and its associated shear instability in the upper 200 m (see Table C1A3).

Table C1A3: *Strength of baroclinic tidal and mean baroclinic currents.*

Stations	IT amplitudes (cm s^{-1}; maximum)	Estimated number of IT eigenmodes	IT vertical shears (s^{-2} x 10^{-4}; maximum)	MBC velocities (cm s^{-1}; maximum)	MBC vertical shear (s^{-2} x 10^{-4}; maximum)
$A^b_{S_2}$	35	6-7	5.5	90	1.2
A^b_o	15	4-5	2.5	98	1.7
A^a_s	45	6-7	7.7	30	0.7
$A^a_{o_1}$	25	4	2.0	90	1.2
$A^a_{o_2}$	40	3	7.6	67	1.2
$A^a_{o_3}$	25	3	3.3	69	1.3
A_{isw}	40	4.5	5.0	71	1.1
Eo	15	4	3.5	43	2.7
Es	20	4	1.2	28	0.8

~~**SD** = Standard Deviation.~~

Formatted: Superscript
Formatted: Superscript
Formatted: Superscript
Formatted: Superscript
Formatted: Superscript
Formatted: Subscript

Data availability

The AMAZOMIX data can be downloaded directly on the SEANOE site: https://www.seanoe.org/data/00860/97235/. The NEMOv3.6 model outputs are available upon request by contacting the corresponding author.

Authors contributions

AKL: funding acquisition. FK and AKL, with assistance from JM: conceptualization and methodology. FK, with assistance from PR, AB, EC, and AKL: data pre-processing. Formal analysis: FK with interactions from all co-authors. Preparation of the manuscript: FK with contributions from all co-authors. This work is a contribution to the LMI TAPIOCA (www.tapioca.ird.fr).

Competing interests

The authors declare that they have no conflict of interest.

Acknowledgments

The authors thank the "Flotte Océanographique Française" and the officers and crew of the R/V Antea for their contributions to the success of operations aboard the vessel. We also appreciate the scientists involved in data and water sample collection for their valuable support during and after the AMAZOMIX cruise. We acknowledge the Brazilian authorities for authorizing the survey. The authors also thank Rockland for providing their instrument and support during the cruise and VMP data analysis,

the French National Instrument Park (DT-INSU) for supplying equipment and assisting with data analysis, and US-IMAGO from IRD for its help during the cruise and in biogeochemical data analysis.

Financial support

This work is part of the "AMAZOMIX" project, funded by multiple agencies: the "Flotte Océanographique Française," which supported the 40 days at sea aboard the R/V Antea; the Institut de Recherche pour le Développement (IRD), including the LMI TAPIOCA program; CNES, through the APR TOSCA MIAMAZ TOSCA project (PIs Ariane Koch-Larrouy, Vincent Vantrepotte, and Isabelle Dadou); LEGOS; and the Franco-Brazilian program GUYAMAZON (Call Nº 005/2017). It is also part of the PhD thesis of Fabius Kouogang, funded by Coordenação de Aperfeiçoamento de Pessoal de Nível Superior (CAPES), under the co-advisement of Ariane Koch-Larrouy and Moacyr Araujo. Co-authors Moacyr Araujo and Alex Costa da Silva acknowledge the Brazilian funding agency CNPq (National Council for Scientific and Technological Development) for their grants.

References

Assene, F., Koch-Larrouy, A., Dadou, I., Tchilibou, M., Morvan, G., Chanut, J., Costa da Silva, A., Vantrepotte, V., Allain, D., and Tran, T.-K.: Internal tides off the Amazon shelf – Part 1: The importance of the structuring of ocean temperature during two contrasted seasons, Ocean Sci., 20, 43–67, https://doi.org/10.5194/os-20-43-2024, 2024.

Assuncao, R. V., Silva, A. C., Roy, A., Bourlès, B., Silva, C. A. H. S., Ternon, J.-F., Araujo, M., and Bertrand, A.: 3D characterisation of the thermohaline structure in the southwestern tropical Atlantic derived from functional data analysis of in situ profiles, Progress in Oceanography, 187, pp.102399, https://doi.org/10.1016/j.pocean.2020.102399. hal02984588, 2020.

Barbot, S., Lyard, F., Tchilibou, M., and Carrere, L.: Background stratification impacts on internal tide generation and abyssal propagation in the western equatorial Atlantic and the Bay of Biscay, Ocean Sci., 17, 1563–1583, https://doi.org/10.5194/os-17-1563-2021 , 2021.

Barnier, B., Reynaud, T., Beckmann, A., Böning, C., Molines, J.-M., Barnard, S., and Jia, Y.: On the seasonal variability and eddies in the North Brazil Current: insights from model intercomparison experiments, Prog. Oceanogr., 48, 195–230, https://doi.org/10.1016/S0079-6611(01)00005-2, 2001.

Bertrand, A., de Saint Leger, E., and Koch-Larrouy, A.: AMAZOMIX 2021 cruise, RV Antea, https://doi.org/10.17600/18001364, 2021.

Booth, J. and Kamenkovich, I.: Isolating the role of mesoscale eddies in mixing of a passive tracer in an eddy resolving model, J. Geophys. Res., 113, C05021, https://doi.org/10.1029/2007JC004510, 2008.

Bordois, L.: Internal tide modeling : Hydraulic & Topographic controls, Ph.D. thesis, Université Toulouse III Paul-Sabatier, 195 pp., tel-01281760, version 1., https://theses.hal.science/tel-01281760, 2015.

Bourlès, B., Gouriou, Y., and Chuchla, R.: On the circulation in the upper layer of the western equatorial Atlantic, Journal of Geophysical Research, 104, 21151-21170, https://doi.org/10.1029/1999JC900058, 1999.

Bouruet-Aubertot, P., Cuypers, Y., Ferron, B., Dausse, D., Ménage, O., Atmadipoera, A. S., and Jaya, I.: Contrasted turbulence intensities in the Indonesian Throughflow: a challenge for parameterizing energy dissipation rate, Ocean Dynamics, 68, 779–800, https://doi.org/10.1007/s10236-018-1159-3, 2018.

Brainerd, K., and Gregg M. C.: Surface mixed and mixing layer depths, Deep Sea Res., 42(9), 1521–1543, https://doi.org/10.1016/0967-0637(95)00068-H, 1995.

Brandt, P., Rubino, A., and Fischer, J.: Large-amplitude internal solitary waves in the North Equatorial Countercurrent. Journal of Physical Oceanography, 32(5), 1567–1573. https://doi.org/10.1175/1520-0485(2002)032<1567:LAISWI>2.0.CO;2, 2002.

Cisewski, B., Strass, V. H., Losch, M., and Prandke, H.: Mixed layer analysis of a mesoscale eddy in the Antarctic Polar Front Zone, J. Geophys. Res., 113, C05017, https://doi.org/10.1029/2007JC004372, 2008.

Coles, V. J., Brooks, M. T., Hopkins, J., Stukel, M. R., Yager, P. L., and Hood, R. R.: The pathways and properties of the Amazon River Plume in the tropical North Atlantic Ocean, Journal of Geophysical Research, 118, 6894-6913, https://doi.org/10.1002/2013JC008981, 2013.

de Boyer Montégut, C., Madec G., Fischer A. S., Lazar A., and Iudicone D.: Mixed layer depth over the global ocean: An examination of profile data and a profile-based climatology, J. Geophys. Res., 109, C12003, https://doi.org/10.1029/2006JC004051, 2004.

de Macedo, C. R., Koch-Larrouy, A., da Silva, J. C. B., Magalhães, J. M., Assene, F., Tran, M. D., Dadou, I., M'hamdi, A., Tran, T. K., and Vantrepotte, V.: Internal tide signatures on surface chlorophyll concentration in the Brazilian Equatorial Margin. Submitted, 2025.

de Macedo, C. R., Koch-Larrouy, A., da Silva, J. C. B., Magalhães, J. M., Lentini, C. A. D., Tran, T. K., Rosa, M. C. B., and Vantrepotte, V.: Spatial and temporal variability in mode-1 and mode-2 internal solitary waves from MODIS-Terra sun glint off the Amazon shelf, Ocean Sci., 19, 1357–1374, https://doi.org/10.5194/os-19-1357-202, 2023.

Dossa, N., da Silva, A. C., Koch-Larrouy, A., and Kouogang, F.: Near-surface western boundary circulation off the Amazon Plume from AMAZOMIX data, in preparation, 2025.

Fer, I., Dengler, M., Holtermann, P. et al.: ATOMIX benchmark datasets for dissipation rate measurements using shear probes, Sci Data, 11, 518, https://doi.org/10.1038/s41597-024-03323-y, 2024.

Fratantoni, D. M. and Glickson, D. A.: North Brazil Current Ring Generation and Evolution Observed with SeaWiFS, J. Phys. Oceanogr., 32, 1058–1074, https://doi.org/10.1175/1520-0485(2002)032<1058:NBCRGA>2.0.CO;2, 2002.

Garrett, C. and Kunze, E.: Internal tide generation in the deep ocean. Annual Review of Fluid Mechanics, 39(1), 57–87. https://doi.org/10.1146/annurev.fluid.39.050905.110227, 2007.

Geyer, W. R.: Tide-induced mixing in the Amazon Frontal Zone, J. Geophys. Res., 100, 2341, https://doi.org/10.1029/94JC02543, 1995.

Gille, S.T., Ledwell, J., Naveira-Garabato, A., Speer, K., Balwada, D., Brearley, A., Girton, J.B., Griesel, A., Ferrari, R., Klocker, A., LaCasce, J., Lazarevich, P., Mackay, N., Meredith, M.P., Messias, M.-J., Owens, B., Sallée, J.-B., Sheen, K., Shuckburgh, E., Smeed, D. A., St. Laurent, L.C., Toole, J.M., Watson, A.J., Wienders, N., and Zajaczkovski, U.: The diapycnal and isopycnal mixing experiment: a first assessment, CLIVARExchanges, 17(1), 46–48, https://nora.nerc.ac.uk/id/eprint/18245, 2012.

Gregg, M., Sanford, T., and Winkel, D.: Reduced mixing from the breaking of internal waves in equatorial waters, Nature, 422, 513–515, https://doi.org/10.1038/nature01507, 2003.

Hersbach, H., Bell, B., Berrisford, P., Hirahara, S., Horányi, A.,Muñoz-Sabater, J., Nicolas, J., Peubey, C., Radu, R., Schepers, D., Simmons, A., Soci, C., Abdalla, S., Abellan, X., Bal-samo, G., Bechtold, P., Biavati, G., Bidlot, J., Bonavita, M., DeChiara, G., Dahlgren, P., Dee, D., Diamantakis, M., Dragani, R.,Flemming, J., Forbes, R., Fuentes, M., Geer, A., Haimberger,L., Healy, S., Hogan, R.J., Hólm, E., Janisková, M., Keeley, S.,Laloyaux, P., Lopez, P., Lupu, C., Radnoti, G., de Rosnay, P.,Rozum, I., Vamborg, F., Villaume, S., and Thépaut, J.-N.: The ERA5 global reanalysis, Q. J. Roy. Meteor. Soc., 146, 1999–2049, https://doi.org/10.1002/qj.3803, 2020.

Huang, P.-Q., Cen, X.-R., Lu, Y.-Z., Guo, S.-X., and Zhou, S.-Q.: Global distribution of the oceanic bottom mixed layer thickness, Geophysical Research Letters, 46, 1547–1554, https://doi.org/10.1029/2018GL081159, (2019).

Huthnance, J. M.: Circulation, exchange and water masses at the ocean margin: the role of physical processes at the shelf edge, Progress in Oceanography, 35, 353–431, https://doi.org/10.1016/0079-6611(95)80003-C, 1995.

Inall, M. E., Toberman, M., Polton, J. A., Palmer, M. R., Green, J. A. M., and Rippeth, T. P.: Shelf Seas Baroclinic Energy Loss: Pycnocline Mixing and Bottom Boundary Layer Dissipation, Journal of Geophysical Research: Oceans, 126(8):2020JC016528, https://doi.org/10.1029/2020JC016528, 2021.

Ivey, G. N., Bluteau, C. E., Gayen, B., Jones, N. L., and Sohail, T.: Roles of Shear and Convection in Driving Mixing in the Ocean, Geophysical Research Letters, 48(3), e2020GL089455, https://doi.org/10.1029/2020GL089455, 2021.

Jackson, C. R., da Silva, J. C. B., and Jeans, G.: The generation of nonlinear internal waves, Oceanography, 25(2):108–123, https://doi.org/10.5670/oceanog.2012.46, 2012.

Johns, W. E., Lee, T. N., Beardsley, R. C., Candela, J., Limeburner, R., and Castro, B.: Annual Cycle and Variability of the North Brazil Current. Journal of Physical Oceanography, 28(1), 103-128. https://doi.org/10.1175/1520-0485(1998)028<0103:ACAVOT>2.0.CO;2, 1998.

Johns, W. E., Lee, T. N., Beardsley, R. C., Candela, J., Limeburner, R., and Castro Filho, B. M. : Annual Cycle and Variability of the North Brazil Current, Journal of Physical Oceanography, 28(1), 103-128, https://doi.org/10.1175/15200485(1998)028%3C0103:acavot%3E2.0.co;2, 1998.

Klymak, J. M., Pinkel, R., and Rainville, L.: Direct breaking of the internal tide near topography: Kaena ridge, hawaii, J. Phys. Oceanogr., 38 (2), 380–399, https://doi.org/10.1175/2007JPO3728.1, 2008.

Koch-Larrouy, A., Atmadipoera, A., van Beek, P., Madec, G., Aucan, J., Lyard, F., Grelet, J., and Souhaut, M.: Estimates of tidal mixing in the Indonesian archipelago from multidisciplinary INDOMIX in-situ data, Deep Sea Research Part I: Oceanographic Research Papers, 106, pp.136-153, https://doi.org/10.1016/j.dsr.2015.09.007, 2015.

Koch-Larrouy, A., Lengaigne, M., Terray, P., Madec, G., and Masson, S.: Tidal mixing in the Indonesian Seas and its effect on the tropical climate system, Clim. Dynam., 34, 891–904, https://doi.org/10.1007/s00382-009-0642-4, 2010.

Kunze, E.: The internal-wave-driven meridional overturning circulation, J. Phys. Oceanogr., 47, 2673–2689, https://doi.org/10.1175/JPO-D-16-0142.1, 2017.

Lellouche, J.-M., Greiner, E., Le Galloudec, O., Garric, G., Reg-nier, C., Drevillon, M., Benkiran, M., Testut, C.-E., Bourdalle-Badie, R., Gasparin, F., Hernandez, O., Levier, B., Drillet, Y.,Remy, E., and Le Traon, P.-Y.: Recent updates to the Copernicus Marine Service global ocean monitoring and forecasting real-time 1/12◦ high-resolution system, Ocean Sci., 14, 1093–1126,https://doi.org/10.5194/os-14-1093-2018, 2018.

Lozovatsky, I. D., Roget, E., Fernando, H. J. S., Figueroa, M., and Shapovalov, S.: Sheared turbulence in a weakly stratified upper ocean, Deep Sea Res. Part I, 53, 387–407, https://doi.org/10.1016/j.dsr.2005.10.002, 2006.

Lueck, R., Fer, I., Bluteau, C., Dengler, M., Holtermann, P., Inoue, R., LeBoyer, A., Nicholson, S., Schulz, K., and Stevens, C.L: Best practices recommendations for estimating dissipation rates from shear probes, Frontiers in Marine Science, https://doi.org/10.3389/fmars.2024.1334327, 2024.

Lyard, F. H., Allain, D. J., Cancet, M., Carrère, L., and Pi-cot, N.: FES2014 global ocean tide atlas: design and perfor-mance, Ocean Sci., 17, 615–649, https://doi.org/10.5194/os-17-615-2021, 2021.

M'hamdi, A., Koch-Larrouy, A., Bosse, A., de Macedo, C., Vantrepotte, V., Dadou, I., da Silva, A. C., and Kouogang, F.: Internal tides imprints on chlorophyll in mesoscale intrathermocline lenses detected from ocean color and from in-situ glider data off the Amazon shelf, in preparation, 2025.

Madec, G., Bourdallé-Badie, R., Chanut, J., Clementi, E., Cow-ard, A., Ethé, C., Iovino, D., Lea, D., Lévy, C., Lo-vato, T., Martin, N., Masson, S., Mocavero, S., Rousset,C., Storkey, D., Vancoppenolle, M., Müeller, S., Nurser, G., Bell, M., and Samson, G.: NEMO ocean engine, Zenodo, https://doi.org/10.5281/zenodo.3878122, 2019.

Magalhaes, J. M., da Silva, J. C. B., Buijsman, M. C., and Garcia, C. A. E.: Effect of the North Equatorial Counter Current on the generation and propagation of internal solitary waves off the Amazon shelf (SAR observations), Ocean Sci., 12, 243–255, https://doi.org/10.5194/os-12-243-2016, 2016.

Miles, J. W.: On the stability of heterogeneous shear flows, Journal of Fluid Mechanics, 10(4):496-508, https://doi.org/10.1017/S0022112061000305, 1961.

Muacho, S., da Silva, J. C. B., Brotas, V., Oliveira, P. B., and Magalhaes, J. M.: Chlorophyll enhancement in the central region of the Bay of Biscay as a result of internal tidal wave interaction, Journal of Marine Systems, 136, 22–30, https://doi.org/10.1016/j.jmarsys.2014.03.016, 2014.

Munk, W., and Wunsch, C.: Abyssal recipes II: Energetics of tidal and wind mixing. Deep Sea Research, Part I: Oceanographic Research Papers, 45, 1977–2010, https://doi.org/10.1016/S0967-0637(98)00070-3, 1998.

Nasmyth, P. W.: Oceanic turbulence, Ph.D. thesis, University of British Columbia, 71 pp, https://doi.org/10.14288/1.0084817, 1970.

Neto, A. V. N., and da Silva, A. C.: Seawater temperature changes associated with the North Brazil current dynamics, Ocean Dynamics, 64, 13–27, https://doi.org/10.1007/s10236-013-0667-4, 2014.

New, A. L., and Pingree, R. D.: Local Generation Of Internal Soliton Packets In The Central Bay Of Biscay, Deep-Sea Research Part A-Oceanographic Research Papers, 39 (9A), 1521 - 1534, https://doi.org/10.1016/0198-0149(92)90045-U, 1992.

New, A., and da Silva, J.: Remote-sensing evidence for the local generation of internal soliton packets in the central Bay of Biscay, Deep Sea Research Part I: Oceanographic Research Papers, 49, 915–934, https://doi.org/10.1016/S09670637(01)00082-6, 2002.

Noh, Y., Lee, WS.: Mixed and mixing layer depths simulated by an OGCM, J. Oceanogr., 64, 217–225, https://doi.org/10.1007/s10872-008-0017-1, 2008.

Rainville, L., and Pinkel, R.: Propagation of Low-Mode Internal Waves through the Ocean, Journal of Physical Oceanography, 36:1220, 2006, https://doi.org/10.1175/JPO2889.1, 2006.

Ruault, V., Jouanno, J., Durand, F., Chanut, J., and Benshila, R.: Role of the Tide on the Structure of the Amazon Plume: A Numerical Modeling Approach, J. Geophys. Res.-Oceans, 125, e2019JC015495, https://doi.org/10.1029/2019JC015495, 2020.

Silva, J. D., Buijsman, M. C., and Magalhaes, J.: Internal waves on the upstream side of a large sill of the Mascarene Ridge: a comprehensive view of their generation mechanisms and evolution, Deep Sea Research Part I: Oceanographic Research Papers, 99, 87-104, https://doi.org/10.1016/j.dsr.2015.01.002, 2015.

Simpson, J. H., and Sharples, J.: Introduction to the physical and biological oceanography of shelf seas, Cambridge University Press, pp. 1-24, https://doi.org/10.1038/250404a0, 2012.

Solano, M. S., Buijsman, M. C., Shriver, J. F., Magalhaes, J., da Silva, J., Jackson, C., Arbic, B. K., and Barkan, R.: Nonlinear internal tides in a realistically forced global ocean simulation, Journal of GeophysicalResearch: Oceans, 128, https://doi.org/10.1029/2023JC019913, 2023.

Stansfield, K., Garrett, C., Dewey, R.: The probability distribution of the Thorpe displacement within overturns in Juan de Fuca Strait, J. Phys. Oceanogr, 31, 3421–3434, https://doi.org/10.1175/1520-0485(2001)031<3421:TPDOTT>2.0.CO;2, 2001.

Sutherland, G., Reverdin, G., Marié, L., and Ward, B.: Mixed and mixing layer depths in the ocean surface boundary layer under conditions of diurnal stratification, Geophys. Res. Lett, 41, 8469–8476, https://doi.org/10.1002/2014GL061939, 2014.

Takahashi, A., and Hibiya, T.: Assessment of finescale parameterizations of deep ocean mixing in the presence of geostrophic current shear: Results of microstructure measurements in the Antarctic Circumpolar Current region, Journal of Geophysical Research: Oceans, 124, 135–153, https://doi.org/10.1029/2018JC014030, 2019.

Tchilibou, M., Koch-Larrouy, A., Barbot, S., Lyard, F., Morel, Y., Jouanno, J., and Morrow, R.: Internal tides off the Amazon shelf during two contrasted seasons: Interactions with background circulation and SSH imprints, Ocean Science Discussions, 14, 1283–1301, https://doi.org/10.5194/os-18-1591-2022, 2022.

Thorpe, S. A.: Models of energy loss from internal waves breaking in the ocean, Journal of Fluid Mechanics, 836, 72–116, https://doi.org/10.1017/jfm.2017.780, 2018.

Whalen, C. B., Talley, L. D., and MacKinnon, J. A.: Spatial and temporal variability of global ocean mixing inferred from Argo profiles, Geophys. Res. Lett, 39:L18612, https://doi.org/10.1029/2012GL053196, 2012.

Xie, X. H., Cuypers, Y., Bouruet-Aubertot, P., Ferron, B., Pichon, A., Lourenço, A., and Cortes, N.: Large-amplitude internal tides, solitary waves, and turbulence in the central Bay of Biscay, Geophysical Research Letters, 40(11), 2748–2754, https://doi.org/10.1002/grl.50533, 2013.

Xu, P., Yang, W., Zhu, B., Wei, H., Zhao, L., and Nie, H.: Turbulent mixing and vertical nitrate flux induced by the semidiurnal internal tides in the southern Yellow Sea, Continental Shelf Research, 208, 104240, https://doi.org/10.1016/j.csr.2020.104240, 2020.

Zhao, Z., Alford, M. H., and Girton, J.B.: Mapping low-mode internal tides from multisatellite altimetry, Oceanography, 776 25(2):42–51,https://doi.org/10.5670/oceanog.2012.40, 2012.

Zhao, Z., Alford, M. H., Girton, J. B., Rainville, L., and Simmons, H. L.: Global Observations of Open-Ocean Mode-1 M2 Internal Tides, J. Phys. Oceanogr., 46, 1657–1684, https://doi.org/10.1175/JPO-D-15-0105.1, 2016